ABSTRACT

NARENDRA, NAMITA. Multiscale Modelling of Electronic and Thermal Transport : Thermoelectrics, Turbostratic 2D Materials and Diamond/c-BN HEMT. (Under the direction of Prof. Ki Wook Kim.)

Multiscale modelling has become necessary with the advent of low dimensional devices as well as use of heterostructures which necessitates atomistic treatment of the interfaces. Multiscale methodology is able to capture the quantum mechanical atomistic details while enabling the simulation of micro-scale structures at the same time. In this thesis, multiscale modelling has been applied to study transport in thermoelectrics, turbostratic 2D MoS_2/WS_2 heterostructure and diamond/c-BN high mobility electron transistor (HEMT).

The possibility of enhanced thermoelectric properties through nanostructuring is investigated theoretically in a p-type Bi_2Te_3/Sb_2Te_3 heterostructure. A multi-scale modeling approach is adopted to account for the atomistic characteristics of the interface as well as the carrier/phonon transport properties in the larger scales. The calculations clearly illustrate the desired impact of carrier energy filtering at the potential barrier by locally boosting the power factor over a sizable distance in the well region. Further, the phonon transport analysis illustrates a considerable reduction in the thermal conductivity at the heterointerface. Both effects are expected to provide an effective means to engineer higher zT in this material system.

Next, power factor enhancement through resonant doping is explored in Bi_2Te_3 based on a detailed first-principles study. Of the dopant atoms investigated, it is found that the formation of resonant states may be achieved with In, Po and Na, leading potentially to significant increase in the thermoelectric efficiency at room temperature. While dop-

ing with Po forms twin resonant state peaks in the valence and conduction bands, the incorporation of Na or In results in the resonant states close to the valence band edge. Further analysis reveals the origin of these resonant states. Transport calculations are also carried out to estimate the anticipated level of enhancement.

Next, in-plane and cross-plane transport in turbostratic MoS_2/WS_2 heterostructure is investigated. Since it is a major challenge in controlling the stacking orientation while growing these heterostructures, the electronic transport properties can experience a sizeable impact via misorientation. Small rotation angles lead to large unit cells with thousands of atoms necessiating an analytical tight binding approach. Tight binding model is developed for MoS_2/WS_2 heterostructure by fitting to DFT data which is extended to the turbostratic case. Cross-plane electronic transport is then analyzed by NEGF and Landauer formalism. It is found that in-plane transport remains largely unaffected, while inter-layer electrical resistance increases upto 10% for holes and 30% for electrons.

Finally, diamond/c-BN HEMT is proposed. Diamond is a promising material for high-power electronic applications in both the dc and rf domains. However, the predicted advantages are yet to be realized due to a number of technical challenges. In particular, n-type devices have not been feasible due to the large ionization energies and low thermodynamic solubility limits of n-dopants. Motivated by the recent advances in nonequilibrium processing, we propose and theoretically examine a diamond/c-BN HEMT that can circumvent the critical limitations. A first-principles calculation suggests the desired type-I alignment at the heterojunction of these two nearly lattice matched semiconductors. The investigation also illustrates that a large sheet carrier density in excess of 5×10^{12} cm^{-2} can be induced in the undoped diamond channel by the gate bias. A subsequent analysis of a simple prototype design indicates that the proposed device can achieve large current drive ($\sim$ 10 A/cm), low R_{on} ($\sim$ 0.05 m$\Omega \cdot$ cm^2), and high f_T

($\sim$ 300 GHz) simultaneously.

Multiscale Modelling of Electronic and Thermal Transport : Thermoelectrics, Turbostratic 2D Materials and Diamond/c-BN HEMT

by
Namita Narendra

A dissertation submitted to the Graduate Faculty of
North Carolina State University
in partial fulfillment of the
requirements for the Degree of
Doctor of Philosophy

Electrical Engineering

Raleigh, North Carolina

2017

APPROVED BY:

Prof. Mehmet C. Ozturk	Prof. Daryoosh Vashaee
Prof. David E. Aspnes	Prof. Ki Wook Kim Chair of Advisory Committee

DEDICATION

To the pursuit of scientific knowledge ranging from the subatomic world to the vast galaxies and beyond.

BIOGRAPHY

Namita Narendra was born in Bangalore, India in 1988. She gradauted with a Bachelor of Engineering degree in Electronics and Communication from RVCE, Bangalore, India in May 2010. She then worked for a year in Microsoft and Indian Institute of Science (IISc), Bangalore. She later joined North Carolina State University (NCSU) for MS in Electrical Engineering in August 2011. Upon graduating in December 2012, she started pursuing her PhD under the direction of Dr Ki Wook Kim in Nanoscale Quantum Engineering group.

ACKNOWLEDGEMENTS

I would like to thank my advisor, Dr Ki Wook Kim, for providing me the opportunity to work on interesting problems and learn a lot. His guidance and tremendous knowledge has helped to shape me into a better researcher. I would like to thank Dr Daryoosh Vashaee for guiding me on the thermoelectric research problems and providing invaluable advice. I would also like to thank Dr David E Aspnes and Dr Mehmet C Ozturk for agreeing to serve on my committee and providing valuable feedback.

I would like to thank my colleagues, Dr Yuriy Semenov, Dr Byoung Don Kong, Dr Jeffrey Mullen, Dr Xiaodong Li, Dr Rui Mao, Dr Xiaopeng Duan, Dr Zhenghe Jin, Xilai Li and Minghao Pan. They have been very helpful and the discussions have made the lab a lively place to work in.

I would like to thank my friends, family and roommates for their support and friendship through the years. In particular, I would like to thank my parents for providing me with invaluable emotional support, my sister for providing me a listening ear at all times and my grandparents for their encouragement.

TABLE OF CONTENTS

List of Tables . . . . . **vii**

List of Figures . . . . . **viii**

Chapter 1 Introduction **1**
1.1 Multiscale modelling methodology 1
1.2 Thesis outline 4

Chapter 2 Toward enhanced thermoelectric effects in Bi_2Te_3/Sb_2Te_3 heterostructures **7**
2.1 Introduction 7
2.2 Methods 9
2.2.1 Thermal transport 9
2.2.2 Electrical transport 10
2.3 Results and discussion 14
2.3.1 Thermal transport 14
2.3.2 Electrical transport 14
2.3.3 Impact on zT 17
2.4 Summary 18

Chapter 3 Doping induced enhanced density of states in Bismuth Telluride **26**
3.1 Introduction 26
3.2 Methods 28
3.3 Results and discussion 29
3.3.1 DFT results 29
3.3.2 Partial Density of States 30
3.3.3 Formation Energy 32
3.3.4 Charge Density 33
3.3.5 Transport calculations 33
3.4 Summary 35

Chapter 4 Tight binding modelling of in-plane and cross-plane transport in turbostratic MoS_2/WS_2 heterostructure **42**
4.1 Introduction 42
4.2 Tight binding model 44
4.3 Transport in turbostratic MoS_2/WS_2 heterostructure 47
4.3.1 In-plane transport 47
4.3.2 Cross-plane transport 50

4.4 Conclusion 53

Chapter 5 Diamond/c-BN HEMTs for power applications: A theoretical feasibility analysis 70
5.1 Introduction 70
5.2 Results and discussion 72
5.2.1 DFT band offset 72
5.2.2 Device characteristics 73
5.3 Summary 76

Chapter 6 Summary and outlook 83
6.1 Summary 83
6.2 Outlook 85

References 87

LIST OF TABLES

Table 2.1 Parameters for Bi_2Te_3 and Sb_2Te_3 used in the Monte Carlo simulation. $\alpha_{mn,j}$ and α are the effective mass tensor and the nonparabolicity parameter, respectively. v_l and D_{ac} represent the sound velocity and the acoustic phonon deformation potential constant, while $\hbar\omega_{op}$ and D_{op} are the optical phonon energy and the correspondent deformation potential constant. 19

Table 3.1 Formation energy for the dopant atoms in units of eV. 37

Table 4.1 Orbital character of the bands at high symmetry points for monolayer and bilayer MoS_2 as obtained from DFT calculations. 54

Table 4.2 Slater Koster energy integrals $E_{\mu\mu'}$. $E_{\mu\mu'}$ for integrals not expilicilty written can be found by cyclical permutation of μ, μ' and l, m, n. $E_{\mu'\mu} = (-1)^{p_1+p_2} E_{\mu\mu'}$ where p_1 and p_2 are the parities of orbitals μ and μ'. 55

Table 4.3 Two-center Slater-Koster tight binding parmeters obtained for monolayer MoS_2 and WS_2 in units of eV. 56

Table 4.4 Slater-Koster interlayer tight binding parmeters obtained for bilayer MoS_2, WS_2 and MoS_2/WS_2 heterostructure in units of eV. 57

LIST OF FIGURES

Figure 1.1 Schematic representation of multiscale modelling methods. [1] . . 2

Figure 2.1 Electronic band structure of (a) Bi_2Te_3 and (b) Sb_2Te_3 calculated by DFT. 20

Figure 2.2 (a) Electrical conductivity and (b) Seebeck coefficient validated for p-type Bi_2Te_3 for a doping concentration of 1.1×10^{19} cm^{-3}. The experimental data are from Ref. [2]. 21

Figure 2.3 (a) Phonon transmission function and (b) interfacial thermal resistance (versus temperature) in the Bi_2Te_3/Sb_2Te_3 heterostructure. 22

Figure 2.4 Average hole energy as a function of position with respect to the valence band edge in the Bi_2Te_3/Sb_2Te_3 heterostructure at T=300K. The seemingly discontinuous slope in the band profile at the interface is a numerical artifact of the finite mesh size. The chemical potential μ is shown by the thin dashed line. For convenience, both the hole energy and the valence band profile are plotted from the "hole" point of view (i.e., with a reversed sign or orientation). . . 23

Figure 2.5 Hole relaxation length in p-type Bi_2Te_3 as a function of temperature. 24

Figure 2.6 Seebeck coefficient and power factor in the Bi_2Te_3/Sb_2Te_3 heterostructure as a function of position at T=300K. 25

Figure 3.1 Schematic illustration of a Bi_2Te_3 unit cell showing the three inequivalent substitution sites−Bi, ionic Te, and vdW Te. 38

Figure 3.2 (a)-(c) DOS for the 60-atom Bi_2Te_3 supercell doped with In, Po and Na, respectively, compared to undoped Bi_2Te_3. The reference for energy ($E = 0$ eV) corresponds to the VB maximum of undoped Bi_2Te_3. (d)-(f) Partial DOS for the In, Po, and Na (substituting ionic Te) atom, respectively; and (g)-(i) Partial DOS for the neighboring host atoms bonded to In, Po and Na, respectively. 39

Figure 3.3 Electron charge density (in units of $e/bohr^3$) projected onto the x-z plane for Bi_2Te_3 doped with (a) In substituting a Bi atom, (b) Po substituting a Bi atom, and (c) Na substituting an ionic Te atom. 40

Figure 3.4 (a) Power factor versus Fermi energy for Bi_2Te_3 doped with In, Po and Na at T=300 K. (b) Conductivity and Seebeck coefficient versus Fermi energy for Bi_2Te_3 doped with In. The corresponding results for the undoped case are also shown for comparison. 41

Figure 4.1 The minimum number of atoms in a turbostratic MoS_2/WS_2 heterostructure unit cell as a function of angle of rotation. 57

Figure 4.2 Projected bandstructure for (a) Monolayer MoS_2 and (b) Bilayer MoS_2. 58
Figure 4.3 Electronic bandstructure of (a) Monolayer MoS_2 and (b) Monolayer WS_2. 59
Figure 4.4 Electronic bandstructure of (a) Bilayer MoS_2 and (b) Bilayer WS_2. 60
Figure 4.5 Electronic bandstructure of MoS_2/WS_2 heterostructure. 61
Figure 4.6 Electronic bandstructure of turbostratic MoS_2/WS_2 heterostructure for rotation angle of (a) 21.78° and (b) 13.17°. 62
Figure 4.7 Energy at the valence band Γ valley as a function of rotation angle for turbostratic MoS_2/WS_2 heterostructure. 63
Figure 4.8 Schematic of the turbostratic MoS_2/WS_2 heterostructure device used for Green's function calculation. 64
Figure 4.9 k-resolved normalized conductance for perfectly aligned MoS_2/WS_2 heterostructure of different supercell sizes for (a)-(c) E_F=E_V and (d)-(f) E_F=E_C. 65
Figure 4.10 Interfacial electrical resistance for turbostratic MoS_2/WS_2 heterostructure as compared to the perfectly aligned heterostructure as a function of Fermi energy for (a) holes and (b) electrons. 66
Figure 4.11 k-resolved normalized conductance for holes (E_F=E_V) in turbostratic MoS_2/WS_2 heterostructure compared to the perfectly aligned heterostructure of same supercell size for rotation angles of (a) 21.78° and (b) 13.17°. 67
Figure 4.12 k-resolved normalized conductance for electrons (E_F=E_C) in turbostratic MoS_2/WS_2 heterostructure compared to the perfectly aligned heterostructure of same supercell size for rotation angles of (a) 21.78° and (b) 13.17°. 68
Figure 4.13 Current through turbostratic MoS_2/WS_2 heterostructure as a function of bias voltage for (a) holes and (b) electrons. 69

Figure 5.1 Theoretical specific on-resistance versus breakdown voltage for diamond in comparison with 4H-SiC and GaN. 77
Figure 5.2 Planar averaged potential across the (111) diamond/c-BN heterostructure obtained from a DFT calculation. 78
Figure 5.3 Schematic of the proposed diamond/c-BN HEMT prototype. The gate length is 1 μm, while the gate-to-source and gate-to-drain lengths are 1 μm and 2 μm, respectively. 79
Figure 5.4 Calculated conduction band profile and the corresponding electron density in the channel with no gate bias. The activation energy (E_D) for the n-type dopants is also indicated in the c-BN layer. . 80
Figure 5.5 Sheet carrier density as a function of V_{gs} with V_{ds} set to 0 V. . . . 81

Figure 5.6 Output $I_{ds} - V_{ds}$ characteristics obtained at different V_{gs}. The transconductance g_m is estimated at $V_{gs} = 2$ V. 82

Chapter 1

Introduction

1.1 Multiscale modelling methodology

The electronic devices have been continuously shrinking in size over the past two decades and are now in the nanoscale regime. [3] In order to push the devices into becoming faster, more powerful and more energy efficient, architectures beyond conventional FETs and newer materials beyond silicon are being explored. The device designs being explored include ones with reduced dimensions, like heterostructures [4], nanowires [5] and quantum dots [6]. The introduction of interfaces requires atomistic treatment of carrier transport at these interfaces. Reduced dimensions introduce quantum confinement of carriers [7] requiring quantum mechanical treatment of carrier transport. At the same time, classical treatment of carriers is necessary to simulate regions away from the interface.

Parallelly, 2D van der Waals (vdW) materials are being investigated as candidates for optoelectronic devices [8]. The 2D materials of currenty of interest other than graphene include transition metal dichalcogenides [9] and phosphorene [10]. The transistor design for 2D materials normally involve heterostructures and/or tunneling transistors [11].

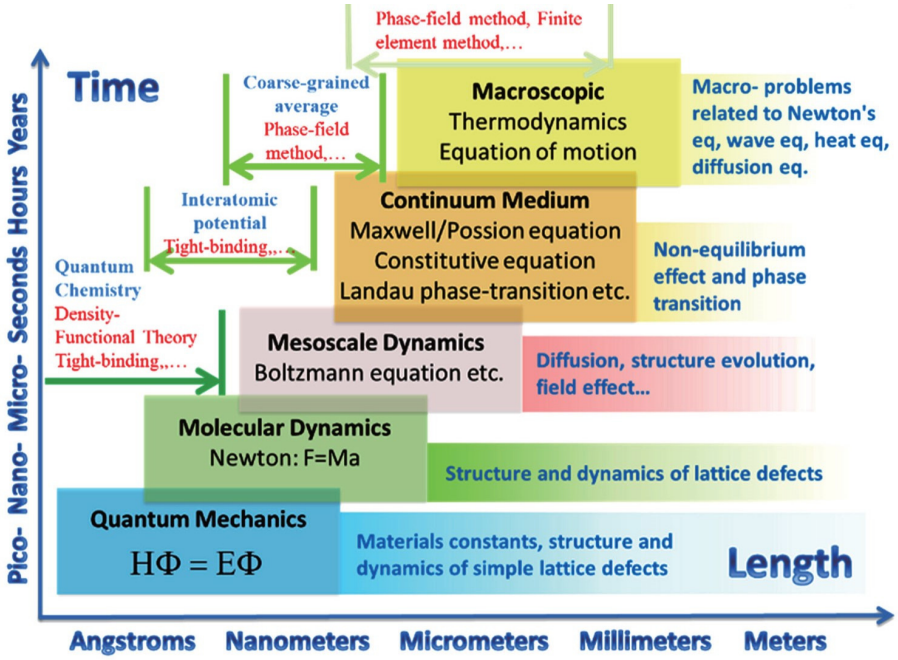

Figure 1.1: Schematic representation of multiscale modelling methods. [1]

Again in these cases, treatment of interfaces becomes very important and classical treatment of electron/phonon transport is insufficient to describe interfaces. However, semi-classical approaches are still relevant for device sizes beyond a few nanometers. Multiscale transport simulation is essential in these scenarios to be able to capture the quantum mechanical atomistic details while enabling the simulation of micro-scale structures at the same time.

Figure 1.1 illustrates the tradeoff involved in selecting the appropriate methodology depending on the length scale of simulation. Ab initio calculations, including density functional theory (DFT), are used to study the crystal structure and extract band information such as effective mass, density of states and scattering rates. In DFT, the Schrödinger equation is solved through the Kohn-Sham formulation. [12] DFT is the method of choice while studying new material systems or extracting interface informa-

tion. While DFT simulations are accurate and includes the atomistic quantum mechanical details, the computational cost is also high. The computational time required for simulating systems beyond a few hundred atoms is prohibitively high. Next up the ladder is molecuar dynamics which can be extended to systems with hundreds of atoms. [13] One of the drawbacks of molecular dynamics is the need for development of interatomic potentials, which is not trivial, especially for new materials which are not well studied. For larger systems, the hamiltonian describing the system can be built by an empirical tight binding approach, [14] whose parameters are fit to reproduce either the ab inito results or experimental data. Once the band structure information is obtained, carrier transport can be formulated in the quantum regime through non-equilibrium Green's function (NEGF) formalism. [15] NEGF is ideal for describing transport in devices in the ballistic regime, in which quantum mechanical effects like size quantization and tunneling can be included. Though scattering can be included in NEGF formalism, it is computationally very intensive. For characterizing transport at the micro-scale, a semi-classical approach is needed. The basis of semi-classical transport is the Boltzmann transport equation (BTE). Monte carlo method allows for direct solution to BTE. [16] Different types of scattering events can be treated very accurately with Monte Carlo approach. However, for devices beyond micro-scale range, Monte Carlo method is not computationally feasible due to the large number of particles needed to be simulated for statistical accuracy. In the meso-scale regime, a macroscopic model like the drift-diffusion model is needed, which is an approximate solution to the BTE. [17]

1.2 Thesis outline

In this thesis, multiscale modelling is applied to study carrier transport in thermoelectrics, turbostratic 2D MoS_2/WS_2 heterostructure and diamond/c-BN high mobility electron transistor (HEMT). In Chapter 2 and Chapter 3, the focus is on thermoelectrics. Thermoelectric devices are devices in which an applied temperature gradient causes diffusion of charge carriers resulting in a built-in voltage. [18] Thermoelectrics have applications in Peltier cooling and waste heat scavenging. The advantage of solid state thermoelectric materials is the absence of moving parts and device scalability. With this, thermoelectric materials can be used in self-powered wearable devices whose functionalities can range from entertainment to health monitoring and diagnosis. But, bulk thermoelectric materials have low efficiency and the power output is limited for low temperature gradients (eg. human skin and environment). In order to be able to use thermoelectrics for wearable devices, it is imperative to maximize the efficiency at room temperatures. Recent material science efforts have been focussed on new class of thermoelectric materials which include skutterutides, clathrates and Zintl phases. [19] But these materials operate at high temperature. Bismuth telluride (Bi_2Te_3) still remains the best thermoelectric material at room temperature. [20] Hence, our efforts in this thesis are focussed on improving the efficiency in the bismuth telluride material system.

The efficiency of thermoelectric materials is characterized by the dimensionless figure of merit, zT defined as $S^2\sigma T/\kappa$, where S is the Seebeck coefficient, σ and κ the electronic and thermal conductivity, respectively, and T the absolute temperature. [21] S, σ and κ are highly correlated, which makes it difficult to increase zT in bulk materials. [19] For example, if the doping concentration is increased to increase σ, S reduces. In addition, the electronic contribution to κ increases, thereby reducing zT. Some of the ways to

optimize zT include reducing device dimensionality so that S, σ and κ can be varied independently. Another appoach is to reduce the denominator, i.e κ, by introducing interfaces through use of heterostructures and nanocomposites. zT can also be increased by optimizing the power factor, $S^2\sigma$, through energy filtering and modification of density of states. [22]

In Chapter 2, we focus on the p-type Bi_2Te_3/Sbi_2Te_3 heterostructure. Energy filtering of the holes at the interface increases the power factor, while simultaneously, phonon scattering at the interface reduces κ, thereby increasing zT. Multiscale modelling is applied to study both electron and phonon transport across the interface. DFT is used to obtain the electronic band structure and band parameters. Electron Monte Carlo is then used to study hole transport in the entire heterostructure. For phonon transport, ab initio provides interatomic force constants hamiltonian for Bi_2Te_3/Sbi_2Te_3 interface. Green's function along with Landauer formalism is then used to obtain the interfacial thermal resistance. In Chapter 3, the focus is on increasing the power factor through modification of density of states in Bi_2Te_3. Probable resonant dopant atoms are studied which can result in resonant states close to either conduction band/valence band edge in Bi_2Te_3. Ab initio DFT is used to obtain density of states for doping Bi_2Te_3 with the candidate dopant atoms. Once the resonant dopant atoms have been identified, BTE is solved to obtain macroscopic transport properties for doped Bi_2Te_3.

In Chapter 4, we study in-plane and cross-plane transport in turbostratic MoS_2/WS_2 heterostructure. In these 2D materials, the weak inter-layer vdW force bonding imposes a major challenge in controlling the stacking orientation while growing heterostructures. The electronic transport properties can experience a sizeable impact via misorientation. Commensurate unit cells need to be built for different angles of rotation. Small rotation angles lead to large unit cells with thousands of atoms. In such cases, DFT calculations

are unrealistic. Tight binding model is developed for MoS_2/WS_2 heterostructure by fitting to DFT data which is extended to the turbostratic case. Cross-plane electronic transport is then analyzed by NEGF and Landauer formalism.

In Chapter 5, diamond/c-BN HEMT is proposed and its performance is evaluated. Diamond is a promising, superior power device material with advantages over existing materials like SiC and GaN. The conduction band alignment of diamond and c-BN is first evaluated from DFT. Drift-diffusion model is then used to evaluate $I-V$ characteristics of micron-scale HEMT transistor. In Chapter 6, summary and outlook for future research is provided.

Chapter 2

Toward enhanced thermoelectric effects in Bi_2Te_3/Sb_2Te_3 heterostructures

2.1 Introduction

The thermoelectric performance of a given material or structure is characterized by the figure of merit zT defined as $S^2\sigma T/\kappa$, where S is the Seebeck coefficient, σ and κ the electronic and thermal conductivity, respectively, and T the absolute temperature.[23] One strategy for enhancing zT from the bulk values is to decouple the electronic and thermal constituents via nanostructuring (e.g., nanocomposites or superlattices).[24, 25] Optimization of the electrical transport represented by the power factor ($S^2\sigma$) is constrained by the interdependence of S and σ.[22] The high doping required for a large σ results in degeneracy of the chemical potential, leading to a low S since the differential conductivity is symmetric with respect to the chemical potential. This particular

challenge may be mitigated by introducing an effective energy filter such as a potential barrier of suitable offset height that can result in asymmetry of the differential conductivity in the well region. A crucial condition is that the length of the well region must be shorter than the carrier relaxation length in order to retain the power factor enhancement. [26] Apart from the electrical transport, the thermal transport also needs to be optimized. Scattering of phonons at the interface can reduce κ through the interfacial thermal resistance. [27]

In Chapter 2, we examine theoretically the impact of heterointerfaces on thermoelectric properties by using the p-type Bi_2Te_3/Sb_2Te_3 structures as an example. As is well known, Bi_2Te_3 is one of the most promising candidates for thermoelectric applications among the bulk materials at room temperature. [20] Both the electrical and thermal transport are analyzed in the heterostructure via a multi-scale approach to identify the conditions for the enhanced zT. First-principles calculation in combination with appropriate transport models, including the Monte Carlo and Green's function methods, enables the simulation of structures at the micro-scale level while preserving the quantum mechanical atomistic details. The theoretical study provides a quantitative understanding of the hot hole relaxation dynamics, elucidating a key factor in the optimum design for the enhanced power factor. Additionally, numerical estimation of the interfacial thermal resistance at the Bi_2Te_3/Sb_2Te_3 interface offers insight in gauging the potential benefit of the engineered structures including the superlattices and nanocomposites.

2.2 Methods

2.2.1 Thermal transport

The thermal transport at Bi_2Te_3/Sb_2Te_3 interface is examined by obtaining the interatomic force constants from density functional perturbation theory using QUANTUM ESPRESSO. [28] Bulk Bi_2Te_3 and Sb_2Te_3 have a rhombohedral crystal structure. Ultrasoft fully relativistic pseudopotentials are used with the generalized gradient approximation to include the spin-orbit effects. To account for the van der Waals interaction, the DFT-D2 correction is also employed. A kinetic energy cutoff of 60 Ry is assumed and the Brillouin zone is sampled with an 8×8×2 grid. The optimized structural parameters are found to be $a = 10.31$ Å, $\cos\alpha = 0.912$ and $a = 10.05$ Å, $\cos\alpha = 0.912$ for Bi_2Te_3 and Sb_2Te_3 respectively. The lattice constant of the Bi_2Te_3/Sb_2Te_3 heterostructure is set to the optimized lattice constant of Bi_2Te_3 resulting in a lattice mismatch of 2.5%. The interface structure is relaxed until the total energy is minimized and the force acting on each atom is less than 10^{-4} Ry. The interfacial separation is 2.43 Å which is essentially identical to the inter-quintuple layer separation in Bi_2Te_3 (2.41 Å), since the Te-Te bonding in both cases is through the weak van der Waals interaction. Once the dynamical matrices are constructed, the phonon transmission function $T_{ph}(\omega)$ can be obtained via the real-space Green's function method and the thermal conductance through the structure is calculated by the Landauer formalism as [29]

$$\kappa_{ph}(T) = \int_0^\infty \frac{d\omega}{2\pi}\hbar\omega T_{ph}(\omega)\left[\frac{\partial n(T,\omega)}{\partial T}\right] , \tag{2.1}$$

where $n(T,\omega)$ is the Bose-Einstein distribution function. Finally the interfacial contribution to the thermal resistance can be extracted from Eq. 2.1 by subtracting the resistance

of the leads. The latter originates from the finiteness in the number of available phonon modes even when the effect of scattering is not considered. Further details of the simulation setup can be found in Ref. [30].

2.2.2 Electrical transport

The multi-scale analysis of electrical transport properties starts with the calculation of the band structure of bulk Bi_2Te_3 and Sb_2Te_3 from first principles within the density functional theory (DFT) framework implemented by the QUANTUM ESPRESSO package using the same pseudopotentials described above. The resulting electronic band structures of Bi_2Te_3 and Sb_2Te_3 are shown in Figure 2.1. The conduction band minimum and the valence band maximum lie on the yz plane of the Brillouin zone. The obtained band gap of 114 meV for Bi_2Te_3 shows good agreement with the experimental value (150 $\pm$ 20 meV) as well as a recent theoretical report (140 meV). [31] However, the calculation for Sb_2Te_3 (49 meV) is substantially smaller than the measured data (280 meV). This is because reliable band gap prediction based on DFT is difficult for low band gap materials. Nevertheless, the discrepancy in the computed band gap does not affect the transport calculations as the experimentally determined numbers are adopted in the analysis.

The effective mass tensors for electrons and holes are evaluated by fitting the band extrema to the ellipsoidal form

$$\alpha_{11}k_1^2 + \alpha_{22}k_2^2 + \alpha_{33}k_3^2 + 2\alpha_{23}k_2k_3 = 2m_0E/\hbar^2, \tag{2.2}$$

where m_0 is the free electron mass, k_1, k_2, k_3 are the wave vector components along the principal axes, and E is the carrier energy. The effective mass tensor extracted for the

top-most valence peak and the lowest conduction band in Bi_2Te_3 and Sb_2Te_3 (Table 2.1) shows good agreement with the measured data. [32]

In the implementation of the transport studies, additional complexities arise as Bi_2Te_3 (Sb_2Te_3) has carrier pockets at six equivalent symmetry points in the Brillouin zone (both holes and electrons) whose principal axes are tilted with respect to the crystalline axes. For the sake of simplicity, only the effective mass tensor α_{ij} in the ellipsoidal coordinate system is shown in Table 2.1. The longitudinal and transverse effective mass components for each of the six carrier pockets is obtained in the rhombohedral coordinate system by the application of a unitary rotatory transformation. [33] The non-parabolic dispersion relation of each carrier pocket [i.e., Eq. 2.2] is further approximated by using the Kane model [34]

$$E_{i,j}(1+\alpha E_{i,j}) = \frac{\hbar^2 k_{x,i,j}^2}{2m_{x,i,j}^*} + \frac{\hbar^2 k_{y,i,j}^2}{2m_{y,i,j}^*} + \frac{\hbar^2 k_{z,i,j}^2}{2m_{z,i,j}^*}, \tag{2.3}$$

where α is the non-parabolicity factor and indices i, j denote the specific pocket $(1, 2, ...6)$ and carrier type (e, h), respectively. The corresponding effective mass $m_{\xi,i,j}^*$ can then be determined, as described above, in the direction ξ of the crystalline axis. The non-parabolicity constants are similarly deduced for both materials (see Table 2.1). Consideration of α may be necessary due to the relatively high carrier energies in the potential well regions.

A Monte Carlo approach is adopted to evaluate the macroscopic thermoelectric transport characteristics based on the parameters deduced from first-principles simulations. Along with the electronic band structure described above, the carrier scattering is accounted for by following the standard treatment as described in the literature. [16] The interaction mechanisms considered are the intravalley inelastic acoustic and optical phonon scattering, and the ionized impurity scattering. The scattering models developed in

Ref. [35] are applied for both Bi_2Te_3 and Sb_2Te_3. The contribution of the polar optical phonon scattering is not included since the scattering rate is negligible compared to the processes considered. Other effects such as interface scattering and the size quantization are not expected to be significant as well. One possible exception may be intervalley scattering. While it is not considered in the present investigation due to the general lack of understanding, this mechanism can potentially be important as the energy separation with the secondary valleys is small. The numerical values of the material parameters used to obtain the scattering rates can be found in the table. In particular, the optical and acoustic phonon deformation potential constants are determined by matching the experimental data available in the literature (see below the discussion related to Figure 2.2 for additional details). [2, 36] The Monte Carlo simulation provides the carrier distribution as a function of the momentum at each location (say, x), with which the desired properties can be calculated.

The distribution function f leads to the transport integrals

$$L_{\xi,j}^{(n)}(x) = q^2 \sum_i \int \tau_{i,j}(E_{i,j},x) v_{\xi,i,j}^2(E_{i,j},x) \left[\frac{E_{i,j}-\mu}{k_B T_j(x)}\right]^n D_{i,j}(E_{i,j},x) \left[-\frac{\partial f(E_{i,j},x)}{\partial E_{i,j}(x)}\right] dE_{i,j} \quad (2.4)$$

for $n = 0, 1, 2, ...$ and $\xi = (x, y, z)$. Here, q is the unit charge, τ^{-1} the scattering rate, v the carrier group velocity, μ the chemical potential, T_j the carrier (j) temperature (or, the average energy), and $D_{i,j}$ the density of states for a single carrier pocket. Clearly, T_j can be deduced from f, while the rest are known a priori (e.g., from the electronic band structure, scattering rates, and doping concentrations). In turn, the position-dependent electrical conductivity (σ) and Seebeck coefficient (S) can be estimated as [37]

$$\sigma_\xi(x) = \sum_{j=(e,h)} \sigma_{\xi,j}(x), \quad \sigma_{\xi,j}(x) = L_{\xi,j}^{(0)}(x); \quad (2.5)$$

$$S_\xi(x) = \frac{\sigma_{\xi,e}(x)S_{\xi,e}(x) + \sigma_{\xi,h}(x)S_{\xi,h}(x)}{\sigma_{\xi,e}(x) + \sigma_{\xi,h}(x)}, \quad S_{\xi,j}(x) = -\frac{k_B}{q}\frac{L^{(1)}_{\xi,j}(x)}{L^{(0)}_{\xi,j}(x)}\,. \tag{2.6}$$

The developed model is subsequently calibrated in the bulk structures through comparison with the measured σ and S. The results plotted in Figure 2.2 show good agreement between the two in a wide range of temperatures with a p-type doping concentration of 1.1×10^{19} cm^{-3}, [2, 36] highlighting the accuracy of the adopted theoretical treatment as well as the extracted parameters such as the band curvatures (i.e., effective masses and nonparabolicity) and the deformation potential constants. The calculation also suggests a sizable anisotropy in the conductivity (i.e., x vs. z directions). In comparison, the Seebeck coefficient is almost isotropic and decreases above 300 K signifying the role of the minority carriers. A similar comparison of Sb_2Te_3 properties has not been made for lack of corresponding measurements.

The Monte Carlo model is then extended to investigate the Sb_2Te_3/Bi_2Te_3 structure consisting of two p-type layers with a single heterointerface between them. To incorporate band bending at the interface, the electrostatic potential is obtained from the Sentaurus TCAD simulator by solving the drift-diffusion equation self-consistently including the effect of non-local tunneling. [38] The transmission probability at the interface is calculated quantum mechanically by solving the Schrödinger equation with the lateral momentum conserved. [39, 26]

2.3 Results and discussion

2.3.1 Thermal transport

To examine the impact of the interface on the phonon or thermal transport at the Bi_2Te_3/Sb_2Te_3 interface, the interfacial thermal resistance (also known as the Kapitza resistance) is calculated by a fully first-principles atomistic approach. Figure 2.3(a) provides the phonon transmission function in the Bi_2Te_3/Sb_2Te_3 system. As shown, phonon transport across the interface is almost unimpeded in the low frequency region except for the phonon modes in the energy range of 4.8-7.8 meV. On the other hand, a near complete block is observed for the high frequency optical modes above 14.7 meV. The corresponding thermal resistance of the Bi_2Te_3/Sb_2Te_3 interface is plotted in Figure 2.3(b). The result exhibits a $1/T$ dependence for temperatures below 50 K and is nearly constant above. The numerical estimate of 4.6×10^{-9} Km^2/W at 300 K roughly corresponds to 11.5 nm of Bi_2Te_3 assuming the bulk resistivity of 0.4 Km/W. This relatively small resistance at the interface may be due to the similarity in the crystal structures of Bi_2Te_3 and Sb_2Te_3 (e.g., the well matched modes) as well as the lack of mass disorder at the boundary (Te-Te bonding). Nevertheless, it seems entirely feasible to increase the thermal resistance by at least tens of percent in a reasonably sized structure by simply introducing a heterointerface. A mode-by-mode analysis indicates that both the longitudinal and transverse branches contribute about evenly toward thermal conduction.

2.3.2 Electrical transport

The electron Monte Carlo model described above is employed to evaluate the transport properties as a function of position in the Sb_2Te_3/Bi_2Te_3 heterostructure. The doping

concentrations are set at 5.2×10^{18} cm^{-3} (Sb_2Te_3) and 4.5×10^{19} cm^{-3} (Bi_2Te_3), respectively. The valence band offset is taken to be 0.1 eV, where Bi_2Te_3 forms the potential well region. Due to the absence of the relevant data in the literature, the electron affinity of the bulk materials is used to estimate the valence band offset at the Bi_2Te_3/Sb_2Te_3 interface. Considering that both materials are reported with comparable affinity values around 4.15 eV, only a small offset may be expected in the conduction band. Hence, a larger portion of the band gap difference is attributed to the valence band profile with a conventional rule of roughly 70/30 split. While the presence of strain in the Sb_2Te_3 layer ($\sim$ 2.5 %) can affect the band alignment as well, the extent of this effect is unknown at the moment. Accordingly a rounded-off number of 100 meV is adopted as a rough approximation. The red solid line in Figure 2.4 illustrates the valence band profile. The holes are injected into the Sb_2Te_3 layer which is far enough removed from the interface to ensure a near-equilibrium energy distribution before reaching the region of interest. In the simulation, this thickness (i.e., Sb_2Te_3) is set at 0.5 μm while Bi_2Te_3 extends the structure by another 0.7 μm.

A key property of interest is the hole energy as a function of position. Once the holes reach the Bi_2Te_3 region, their kinetic energies increase due to the band discontinuity. However, this effect is spatially transient since the holes undergo rapid energy relaxation via phonon interaction to reach equilibrium as can be seen from the blue dashed curve in Figure 2.4. By fitting the decay to an exponential curve (i.e., the 1/e decay), the corresponding energy relaxation length λ for the holes is estimated to be around 140 nm at 300 K. We also analyze the net energy dissipated by the holes for a more detailed understanding. As the holes enter the well region, 75% of the extra kinetic energy is carried away by acoustic phonons, while optical phonons account for the remaining 25%. This is expected since the hole-acoustic phonon scattering rate is about two orders of

magnitude higher than the counterpart with optical phonons in Bi_2Te_3. The energy distribution of the emitted hot acoustic phonons follows a Gaussian profile with the peak at 1.8 meV and the full width at half maximum of 1.4 meV.

Figure 2.5 shows the λ in Bi_2Te_3 as a function of temperature. Both acoustic and optical phonon scattering rates have nearly the same temperature dependence, therefore the ratio of energy lost through acoustic phonons to that via optical phonons remains approximately at a constant 3:1 with respect to temperature. A linear relation appears to hold for λ versus T: i.e., $\lambda = (-0.4T + 260)$ in units of nanometer as shown by the red dashed line in Figure 2.5.

The position dependence in the hole energy distribution, in combination with Eq. 2.5 and Eq. 2.6, provides the Seebeck coefficient as a locally defined quantity. For ease of analysis, the expression for S can be further written as

$$S_{\xi,j}(x) = -\frac{1}{qT_j(x)} \sum_i \frac{\int \sigma_{\xi,j,i}(E_{i,j}, x)(E_{i,j} - \mu) dE_{i,j}}{\int \sigma_{\xi,j,i}(E_{i,j}, x) dE_{i,j}} \,. \tag{2.7}$$

The idea of hot carrier filtering is to make the differential conductivity $\sigma_{\xi,j,i}(E_{i,j}, x)$ asymmetric with respect to the electrochemical potential μ, thereby increasing $S(x)$. [26] As the energy dependence of $\sigma_{\xi,j,i}(E_{i,j}, x)$ is essentially determined by $D_{i,j}(E_{i,j}, x)\left[-\frac{\partial f(E_{i,j},x)}{\partial E_{i,j}(x)}\right]$, a non-thermal distribution with a large hot carrier population can evidently lead to the desired asymmetry.

From Figure 2.6, it is clear that the relaxation in the average hole energy degrades S away from the interface; the enhancement (compared to the bulk Bi_2Te_3 value) is preserved only within the carrier relaxation length. Additionally, the high doping on the Bi_2Te_3 side leads to a high conductivity; i.e., 3000 Ω^{-1}cm^{-1} vs. 168 Ω^{-1}cm^{-1} on the low-doped Sb_2Te_3 side. The combination of the enhanced Seebeck coefficient and the large

Bi_2Te_3 conductivity results in a selective improvement in the power factor in the well region. The estimated enhancement is as large as a factor of six close to the interface. Note that the doping conditions require a judicious selection. For instance, a degenerate level in the barrier region (i.e., Sb_2Te_3) could substantially diminish the asymmetry of the differential conductivity at the interface, resulting in a decreased enhancement in S as mentioned earlier. On the other hand, low doping in the Sb_2Te_3 layer would reduce electrical conductivity and, at the same time, increase the contribution of minority carriers to the transport (which is significant due to the small band gap), causing a degradation in S. Thus, the competing factors must be carefully optimized.

2.3.3 Impact on zT

Thus, a tailored combination of the added thermal resistance at the interface and the local increase in the power factor (i.e., the well region) can result in an enhancement in the overall thermoelectric performance of the structure (superlattices/nanocomposites). The degradation in the electrical conductivity (due to the band bending) in the presence of multiple interface is expected to be minimal compared to the gain in the Seebeck coefficient, thus preserving the increase in the power factor, as has been shown for a single interface. This observation is consistent with the recent experimental reports in the literature where a global increase in zT has been realized with nanoinclusions based on a similar concept. [40, 41] The detailed quantification and understanding of the carrier relaxation dynamics at the heterointerface provides a necessary tool to further optimize the thermoelectric structures.

2.4 Summary

Our calculation illustrates the possibility of power factor enhancement in the Bi_2Te_3/Sb_2Te_3 heterostructure through effective energy filtering at the potential barrier. As the observed effect is spatially transient, the heterolayer dimension must remain much smaller than the carrier energy relaxation length. In the case of p-type Bi_2Te_3, this characteristic length is estimated to be approximately 140 nm at room temperature which is clearly practicable. A similar but less pronounced increase is also obtained in the thermal resistance due to the additional phonon scattering at the interface. By combining the respective improvements in the power factor and the thermal resistance, it is not unreasonable to anticipate a significant enhancement in zT with an optimized geometry. The methodology used in the present analysis can be extended to other related material systems.

Table 2.1: Parameters for Bi_2Te_3 and Sb_2Te_3 used in the Monte Carlo simulation. $\alpha_{mn,j}$ and α are the effective mass tensor and the nonparabolicity parameter, respectively. v_l and D_{ac} represent the sound velocity and the acoustic phonon deformation potential constant, while $\hbar\omega_{op}$ and D_{op} are the optical phonon energy and the correspondent deformation potential constant.

Parameter	Bi_2Te_3	Sb_2Te_3	Parameter	Bi_2Te_3	Sb_2Te_3
$\alpha_{11,h}$	32.3	11.62	$\alpha_{11,e}$	36.02	8.73
$\alpha_{22,h}$	6.4	7.24	$\alpha_{22,e}$	7.18	2.9
$\alpha_{33,h}$	10.3	4.33	$\alpha_{33,e}$	12.01	0.79
$\alpha_{23,h}$	2.1	1.1	$\alpha_{23,e}$	3.1	0.76
α (eV^{-1})	8	2			
D_{ac} (eV)	8	10	D_{op} (eV)	6	7
v_l (m/s)	1870	2900	$\hbar\omega_{op}$ (meV)	15	15

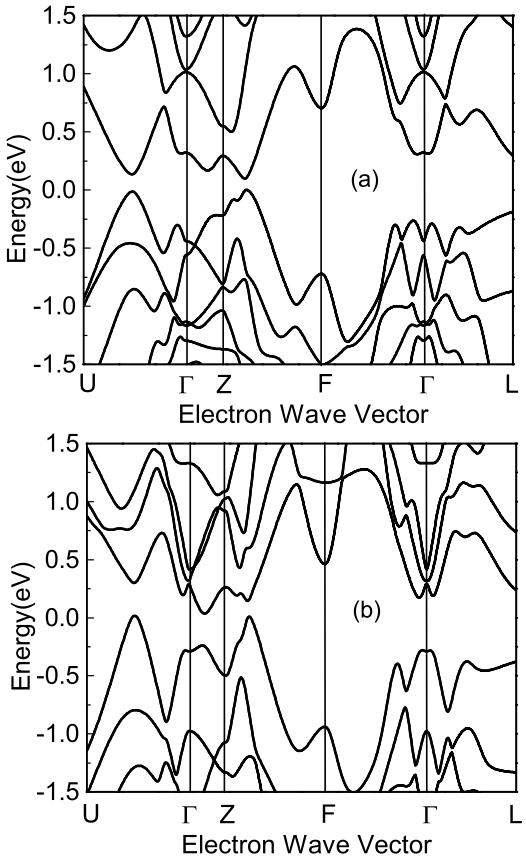

Figure 2.1: Electronic band structure of (a) Bi_2Te_3 and (b) Sb_2Te_3 calculated by DFT.

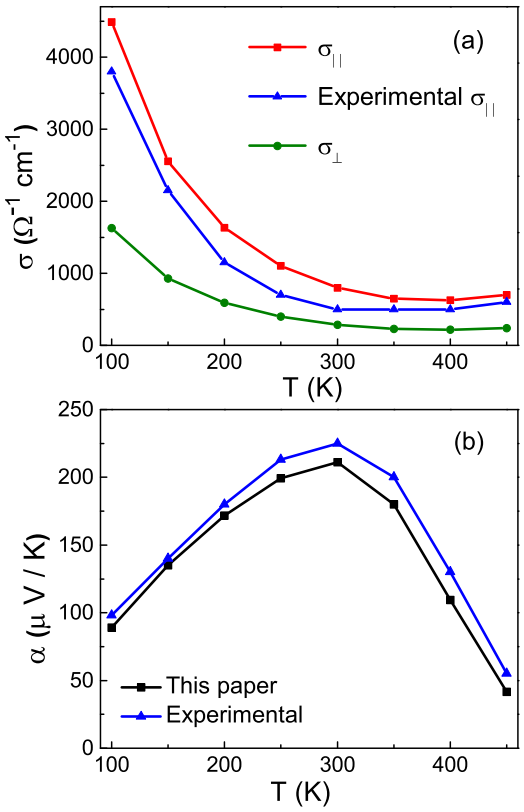

Figure 2.2: (a) Electrical conductivity and (b) Seebeck coefficient validated for p-type Bi_2Te_3 for a doping concentration of 1.1×10^{19} cm^{-3}. The experimental data are from Ref. [2].

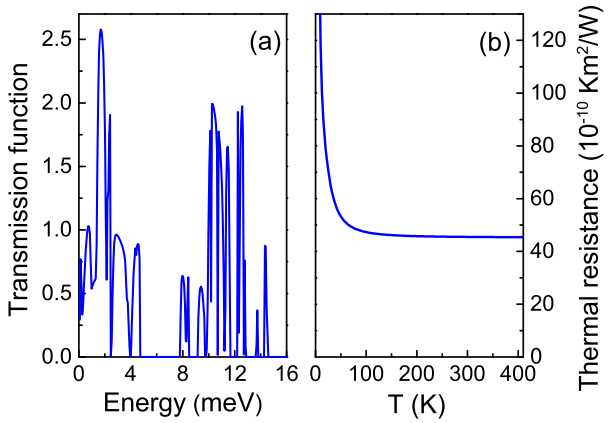

Figure 2.3: (a) Phonon transmission function and (b) interfacial thermal resistance (versus temperature) in the Bi_2Te_3/Sb_2Te_3 heterostructure.

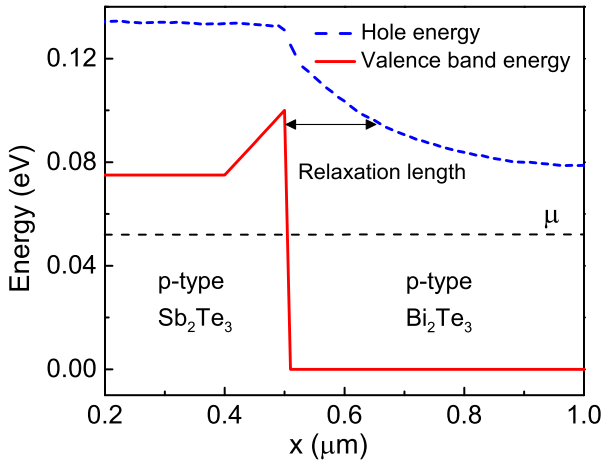

Figure 2.4: Average hole energy as a function of position with respect to the valence band edge in the Bi_2Te_3/Sb_2Te_3 heterostructure at T=300K. The seemingly discontinuous slope in the band profile at the interface is a numerical artifact of the finite mesh size. The chemical potential μ is shown by the thin dashed line. For convenience, both the hole energy and the valence band profile are plotted from the "hole" point of view (i.e., with a reversed sign or orientation).

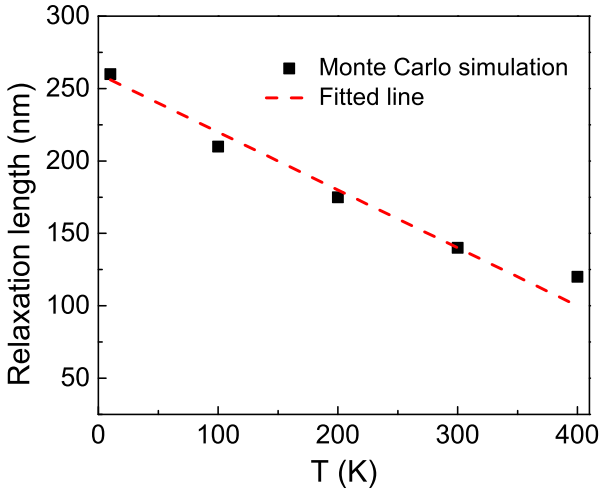

Figure 2.5: Hole relaxation length in p-type Bi_2Te_3 as a function of temperature.

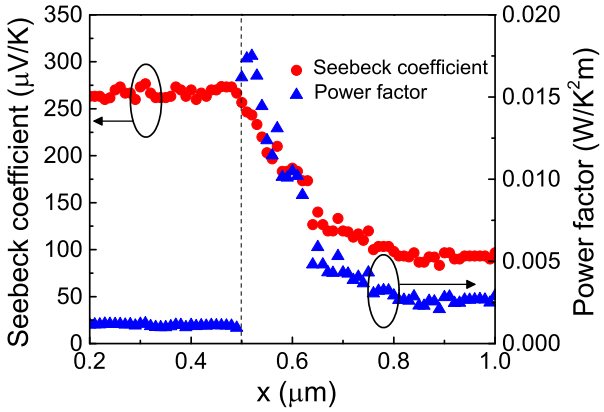

Figure 2.6: Seebeck coefficient and power factor in the Bi_2Te_3/Sb_2Te_3 heterostructure as a function of position at T=300K.

Chapter 3

Doping induced enhanced density of states in Bismuth Telluride

3.1 Introduction

Considerable efforts have been devoted in the recent years to improve the thermoelectric efficiency. The figure of merit zT commonly used to characterize the performance of a given material or structure is defined as $S^2\sigma T/\kappa$, where S is the Seebeck coefficient, σ the electronic conductivity, κ the thermal conductivity, and T the absolute temperature. [21] The strategy to maximize the efficiency can evidently take two paths; viz., optimize κ and/or the power factor term, $S^2\sigma$. The primary focus thus far has been on reducing the lattice contribution to κ through nanostructuring. [42, 43, 44] However, the reduction in κ is constrained both by the electronic thermal conductivity and the fact that the lower bound on the phonon mean free path is the interatomic distance. The alternative route via the power factor is similarly fraught with challenges. In particular, the Seebeck coefficient experiences degradation when enhancement in the conductivity is sought by

increasing the carrier concentration as characterized by the Pisarenko relation. [45] The reduction in S must be avoided since the power factor is proportional to its square.

The potential approaches to circumvent this limiting inter-dependency include band structure engineering through low-dimensional structures, [46, 47] carrier pocket engineering, [48] hot carrier filtering, [49] and introduction of resonant levels. [50, 51] Here, the investigation is focused on the improvement through resonant doping. The Mahan-Sofo theory illustrates that the Seebeck coefficient in a material can be maximized when the density of states (DOS) has a Dirac delta-like peak with the Fermi level aligned $2.4k_BT$ away from the peak and the contributions from the rest of the electronic bands are held at the minimum. [52] While it is impossible to have a Dirac delta function for the DOS, a close approximation is realizable by introducing resonant impurity states through doping of appropriate atoms. In addition, for the resonant level to be conductive as necessary, it is preferable for the impurity state to have a s- or p-like character rather than a highly localized f-like state. The increase in the Seebeck coefficient due to the resonant doping can be quantified by the Mott expression as [53]

$$S = \frac{\pi^2}{3}\frac{k_B^2 T}{q}\left[\frac{g(E)}{n(E)} + \frac{1}{\mu}\frac{d\mu(E)}{dE}\right]_{E=E_f}. \tag{3.1}$$

The first term simply accounts for the increased DOS $g(E)$, whereas the second refers to the increased energy dependence of the mobility $[\mu(E)]$ due to the resonant impurity scattering which is relevant only at low temperatures. Here k_B is the Bolzmann constant, n the carrier density, and E_f the Fermi energy. It should be noted that the Mott relation is derived assuming the transport equation is a smoothly varying function of energy near the Fermi level, and breaks down when there are sharp features in the DOS. Here, since the DOS peaks are not sharp, we may still use the Mott relation. The predicted improvement

in zT as a result of the enhanced local DOS has been experimentally demonstrated in PbTe with 2% doping of Tl. [50] This observation naturally raises a similar prospect for Bi_2Te_3, a material with the highest zT among room-temperature bulk thermoelectrics [20] and thus the focus of significant research interests.

In this chapter, a comprehensive theoretical investigation is undertaken to identify the dopants in bulk Bi_2Te_3 that are likely to realize the resonant states and thus the desired increase in zT. Experimental studies with regards to resonant doping in Bi_2Te_3 have so far shown that doping with Sn increases S which was attributed to the formation of a resonant level in the valence band (VB). [51] On the other hand, no theoretical reports are available in the literature. As part of this work, a fully first-principles approach is adopted to study the doping induced modifications to the DOS for different candidate dopant atoms. Following the initial screening, partial DOS and charge density analyses are carried out for those atoms with promising results. Transport properties are calculated to show the effect of the resonant states on the power factor for doped Bi_2Te_3.

3.2 Methods

The ab initio calculations are performed in the density functional theory (DFT) framework of the plane wave based QUANTUM ESPRESSO. [28] Fully relativistic norm conserving pseudopotentials are used that account for the spin-orbit interaction. Spin polarization, on the other hand, is not considered. The adopted exchange-correlation function is based on the generalized gradient approximation as parametrized by Perdew, Burke and Ernzerhof. [54] The long-ranged van der Waals (vdW) interaction relevant to the material of interest (i.e., Bi_2Te_3) is accounted for by including the semiempirical DFT-D2 correction. [55] The kinetic energy cutoff of 60 Ry along with Methfessel-Paxton smear-

ing of 0.01 Ry is employed. Doped Bi_2Te_3 calculations are carried out by constructing a 60-atom supercell and replacing one of the host atoms with the dopant. The supercell is fully relaxed until the total energy is minimized and the total force on the atoms is less than 10^{-4} Ry. The Brillouin zone is sampled with a (12×12×6) grid. While the cases considered correspond to relatively high doping concentrations ($\sim 4\%$ and $\sim 2.7\%$ for Bi and Te replacement, respectively), a larger supercell is not examined due to the computational constraints. As Bi_2Te_3 has a layered crystal structure with each quintuple layer consisting of two Bi atoms and three Te atoms, three substitutional sites are possible (see Figure 3.1); namely, Bi atom, ionic Te atom (sandwiched between two Bi atoms in the quintuple layer) and vdW Te atom (weakly bonded to Te atom of the next quintuple). Formation energy for each possible combination is evaluated to determine the most energetically favorable substitution site.

3.3 Results and discussion

3.3.1 DFT results

The dopant atoms considered are In, Pb, As, I, Cs, Po, Na, Tl and S. All three substitution sites are considered for each of these dopant atoms. Only the impurity states present within 500 meV of the band edge are of interest since those located outside that energy range are practically irrelevant to the enhancement of thermoelectric power factor. Of the screened dopant atoms, In, Po and Na have resonant peaks in the energy range of interest and are selected for further analysis. Figure 3.2(a) provides the DOS obtained for In atom substituting Bi atom in Bi_2Te_3. As shown, a resonant peak is clearly visible approximately 180 meV away from the VB edge (set at $E = 0$ before doping). The case

of In substituting either kind of Te atom does not exhibit any resonance-like features. Doping with Po also shows favorable results as illustrated in Figure 3.2(b). More interestingly this case introduces, through substituting the Bi atom, twin resonant peaks; one that is 200 meV below the VB edge and the other 80 meV above the conduction band (CB) edge. As with In, no enhancement in the DOS is observed when Po substitutes Te atoms. Finally, the third dopant atom of interest, Na, has a resonant peak 200 meV away from the VB edge [Figure 3.2(c)]. This peak is formed when Na substitutes either kind of Te atom, ionic or vdW, but absent for Na substituting Bi atom. Note that Bi_2Te_3 no longer exhibits a band gap after doping with the resonant atoms in all three cases, while a value of 80 meV is obtained for the pristine case. The disappearance of the band gap is attributed to the large doping density assumed in the calculation (see above). Once the dopant level is lowered sufficiently, the bulk band gap is expected to be restored and the resonant peaks will become narrower and sharper. [56]

3.3.2 Partial Density of States

A partial DOS analysis is carried out to probe the nature or the origin of the resonant peaks which result from the interaction between the wavefunctions of the dopant atoms and those of the host atoms. In a resonant level, the impurity state coincides with the band energy of the host atoms, unlike a normal dopant state where the impurity energy falls within the band gap. For the case of In, the examination reveals that the resonant peak in the VB can be attributed to the s orbital of the dopant [Figure 3.2(d)]. A closer look further suggests sp^3-like hybridization with the neighboring out-of-plane Te atoms, as can be seen from Figure 3.2(g). Partial DOS for Po atom is displayed in Figure 3.2(e). While the VB resonant peak is composed mainly of the p_z orbital of Po, there is an

equal contribution from both p_z and p_{xy} orbitals toward the CB resonant peak. Unlike In, none of the resonant states show hybridized characteristics; instead they are purely p-like states. The analysis also reveals that the Po p-like impurity peaks simply cause an increase in the DOS in the neighboring Te atoms in the same energy range [Figure 3.2(h)], which is associated with a p-like character likewise. An additional point to note is the presence of a very pronounced peak in the impurity p_{xy} orbital centered around 600 meV away from the CB edge [not fully shown in Figure 3.2(e)]. This, however, does not make a significant change for its contribution is nearly shadowed by the large DOS of the host atoms already present in the corresponding energy range [see also Figure 3.2(b)].

As for Na, the origin of the peak differs when Na substitutes either an ionic Te atom or a vdW Te atom. In the case of ionic Te substitution, the VB resonant peak is entirely p-like composed of Na p orbital and Bi p orbital as shown in Figure 3.2(f,i). Here the Na atom modifies the DOS in the neighboring Bi atoms, similar to the Po doping described above. Na has a couple of impurity peaks close to the CB edge arising from p_z and p_{xy} orbital which does not lead to a resonant state due to an overlap between the two peaks resulting in a broadened DOS instead. When Na substitutes a vdW Te atom, on the other hand, the enhanced DOS is due to hybridization between the Na s orbital and the Bi p_z orbital. Since this hybridization is weak, the resonant peak formed is smaller. Note that inclusion of the spin-orbit interaction is essential for accurate description of the resonant states as both Bi and Te p orbitals (which undergo spin-orbit induced energy shift) are involved in the hybridization with impurity atoms.

3.3.3 Formation Energy

To estimate the ease of doping as well as to determine the most stable configuration, the formation energy is calculated for the different substitution sites. Since resonant states are formed only for certain substitution sites, it is essential to determine the most favorable growth condition resulting in the required configuration. The formation energy can be obtained from the following expression; [57]

$$E_{fr} = E^{d}_{\mathrm{Bi_2Te_3}} - E^{ud}_{\mathrm{Bi_2Te_3}} + \Delta n_{\mathrm{Bi}}\mu_{\mathrm{Bi}} + \Delta n_{\mathrm{Te}}\mu_{\mathrm{Te}} - \Delta n_X \mu_X, \tag{3.2}$$

where "d" and "ud" denote the doped and undoped cases, respectively. In addition, Δn_A refers to the number of atoms of species A removed or added to the system with chemical potential μ_A. The chemical potentials for In, Po and Na atoms [denoted as "X" in Eq. 3.2] are readily obtained from the bulk unit cells (with bct, sc, and bcc symmetry, resepctively), as μ in each case corresponds to the total energy of the elemental ground state in the DFT calculation. The values for Bi and Te depend on the growth conditions and must follow the constraint $2\mu_{\mathrm{Bi}} + 3\mu_{\mathrm{Te}} = \mu_{\mathrm{Bi_2Te_3}}$. For the Bi-rich condition, μ_{Bi} is set to its bulk value ($\mathrm{R\bar{3}m}$ symmetry). Correspondingly, μ_{Te} in the Te-rich case is determined likewise ($P3_121$ symmetry). The calculated formation energies for different substitution sites are shown in Table 3.1. When a dopant atom substitutes a Bi atom, it is found that E_{fr} is lower for the Te-rich condition than for the Bi-rich counterpart. The opposite also appears to hold for the case of dopant atom substituting the Te atom. Further, E_{fr} is always lower while substituting a Te vdW site compared to the Te ionic site in both Bi-rich and Te-rich conditions. It is due to the fact that the vdW Te is more loosely bound than the ionic Te and can thus be more easily substituted. For In and Po atoms, the lowest E_{fr} occurs when substituting Bi atom in both Bi-rich and Te-rich

condition. Incidentally, this is the configuration that is predicted with the resonant peaks for both dopants. In the case of Na, replacing a vdW Te atom yields the lowest E_{fr} for the Bi-rich condition, while Bi substitution has lowest E_{fr} for Te-rich condition. Since the resonance peak is observed only for Te substitution, Bi-rich growth is necessary.

3.3.4 Charge Density

The bonding between the dopants and the host atoms is also examined. Figure 3.3 shows the electron charge density along the [010] plane of the Bi_2Te_3 cell for the dopant atoms (In, Po, Na) substituting the host atom. In an ideal Bi_2Te_3 crystal, the bonds between the neighboring intralayer Bi and Te atoms are of a mixed covalent-ionic nature. When In replaces a Bi atom [Figure 3.3(a)], a charge density shift toward the Te atoms (away from the In site) is observed due to the comparatively lower electronegativity of In (vs. Bi). In contrast, Bi substitution by Po depletes the charge density from the neighboring Te atoms resulting in a large electron accumulation around the Po atom as shown in Figure 3.3(b). For both In and Po doping, an enhancement of the ionic nature is observed in the covalent-ionic dopant-Te bond. On the other hand, Na substituting an ionic Te site has a very weak ionic bond with the neighboring Bi atoms. As seen in Figure 3.3(c), the large electronegativity difference between Bi and Na causes complete electron depletion around Na atom. The weak bonding of Na with its neighboring atoms in Bi_2Te_3 is not surprising, given the small size of Na in comparison to Bi and Te.

3.3.5 Transport calculations

It is expected that the resonant peaks formed by proper doping as shown above will increase the power factor and in turn zT of bulk Bi_2Te_3. The effect of these peaks on

the transport properties is quantitatively evaluated by calculating S and σ based on the solution to Boltzmann transport equation in the relaxation time approximation: [37]

$$\sigma = \int \sigma(E)dE, \quad S = -\frac{1}{qT}\frac{\int \sigma(E)(E - E_f)dE}{\int \sigma(E)dE}, \tag{3.3}$$

where q is the unit charge and the differential conductivity $\sigma(E)$ is given by

$$\sigma(E) = q^2\tau(E)v^2(E)g(E)\left[-\frac{\partial f(E)}{\partial E}\right]. \tag{3.4}$$

In the above expression, $\tau^{-1}(E)$ is the scattering rate, $v(E)$ the carrier velocity as the derivative of the dispersion relation along the transport direction, and $f(E)$ the Fermi-Dirac distribution function. For $g(E)$, the DOS obtained from the DFT is used as shown in Figure 3.2(a-c). The total scattering rate is estimated according to Matthiesen's rule accounting for the interactions with acoustic phonon, optical phonon, and ionized impurities, where the directional dependence in the momentum space is ignored. Further details of the scattering calculation and the adopted parameters can be found in Ref. [58]. For the doped Bi_2Te_3, the rate is adjusted to reflect the larger DOS near the band edge (i.e., more scattering). This is achieved by replacing the effective mass in the scattering rate calculation with a value that is extracted from the DOS curve. It is assumed that the increase in the effective mass due to the resonant peaks does not impact the mobility significantly in Bi_2Te_3. [51] A detailed account of the scattering rate with dopant induced states requires first-principles calculation of carrier-phonon interaction as a function of the doping concentration; this is beyond the scope of the current investigation.

The power factor evaluated at 300 K is shown in Figure 3.4(a) as a function of the Fermi energy in the VB. The direction of carrier transport is assumed to be along the

basal plane. Note that the minority carriers are also included in the calculation since Bi_2Te_3 is a low band gap material. The region of interest for E_f is near the resonant peak [0.18 eV away from E_v for In and 0.2 eV for Po and Na; see Figure 3.2(a-c)]. The obtained power factor clearly exhibits a maximum about 2.4 k_BT below the resonant peak position in accordance with the Mahan-Sofo theory (i.e., $E_v - E_f \approx 0.24 - 0.26$ eV). [52] The observed upturn in the power factor is expected to become much larger and sharper for lower doping concentrations as the DOS enhancement will tend to a more Dirac delta-like form; the energy range showing an increase (in the power factor) directly correlates with the broadening of the impurity peak in the DOS. One uncertainty, though, may be with the exact position of the resonant states. While a limited number of simulations conducted in the present study show no evidence of significant shift in energy, a more comprehensive investigation is needed for a definitive answer. A similar observation is made for the resonant peak in the CB with the Po atom. For a more detailed examination, Figure 3.4(b) shows the constituents of the calculated power factor (S and σ) for Bi_2Te_3 doped with In. As illustrated, the enhancement in the power factor near the resonant DOS peak (i.e., $E_v - E_f \approx 0.2 - 0.3$ eV) is predominantly due to the increase in S. In contrast, the observed gain close to the VB edge in Figure 3.4(a) is due to the higher σ that is a consequence of the elevated doping concentration adopted to enable the DFT computation as described earlier. Accordingly this peak in the power factor is not expected to survive at low doping unlike that related to the resonant states.

3.4 Summary

In summary, our DFT study identifies Po as the dopant that can potentially realize the desired resonant peak in the DOS of n-type Bi_2Te_3 while pinpointing In, Po, and

Na for the p-type. The analysis clearly illustrates that these peaks originate from the impurity states of the dopant atom and its interaction with the host atoms. Transport calculations indeed predict the anticipated increase in the power factor that is directly attributed to the resonant features in the DOS. An investigation with a much lower doping concentration for In, Po and Na will help to quantify the precise enhancement in the power factor.

Table 3.1: Formation energy for the dopant atoms in units of eV.

Dopant atom	Substitution site	Formation energy (eV)	
		Bi-rich	Te-rich
In	Bi	-0.52	-0.97
	Te ionic	-0.11	0.18
	Te vdw	-0.37	-0.07
Po	Bi	-0.41	-0.85
	Te ionic	-0.22	0.07
	Te vdw	-0.51	-0.21
Na	Bi	-0.06	-0.38
	Te ionic	-0.28	0.01
	Te vdw	-0.47	-0.17

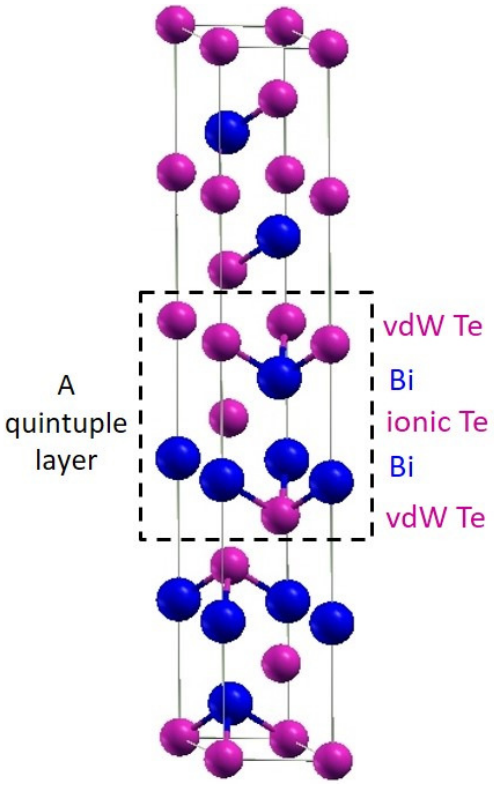

Figure 3.1: Schematic illustration of a Bi_2Te_3 unit cell showing the three inequivalent substitution sites−Bi, ionic Te, and vdW Te.

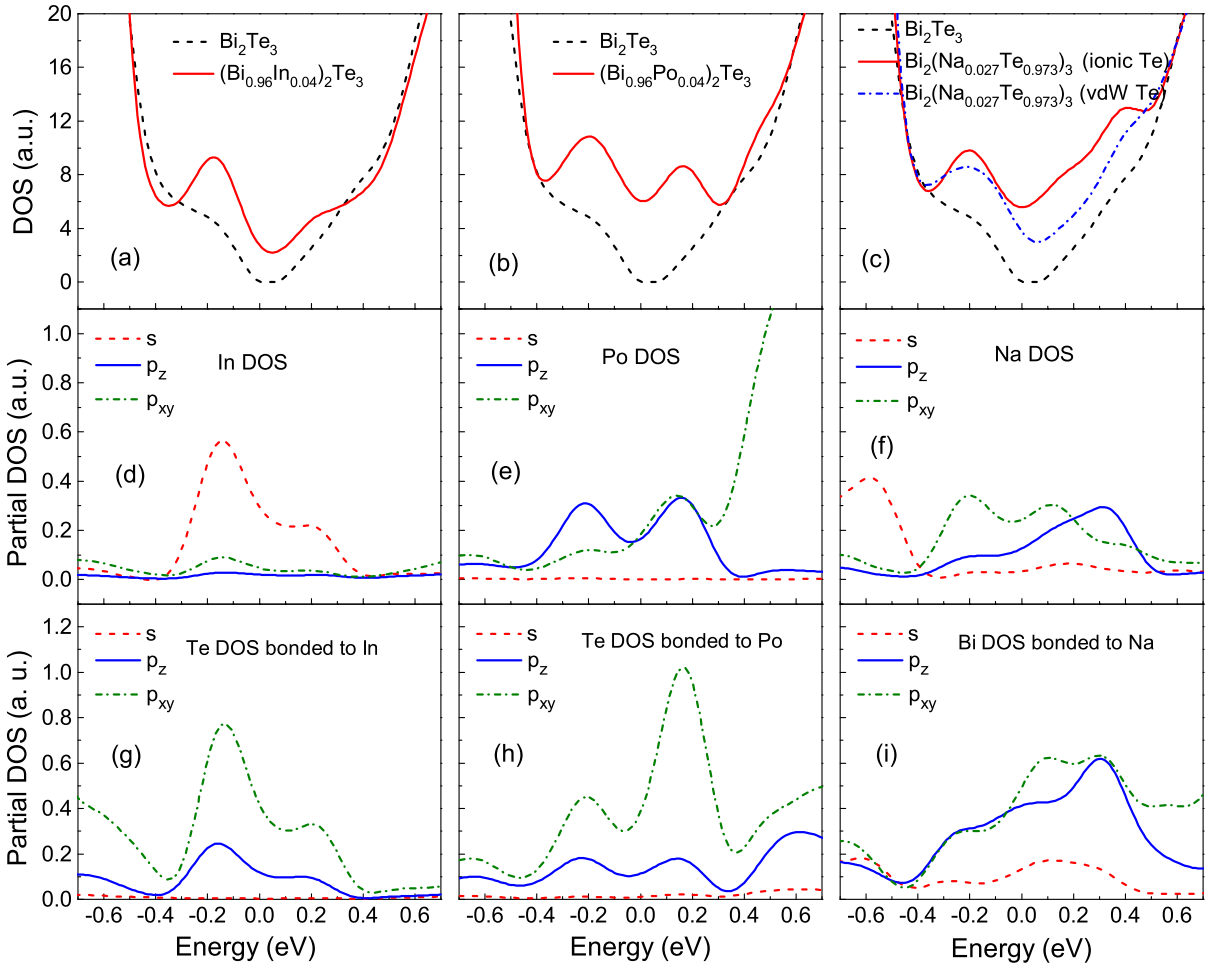

Figure 3.2: (a)-(c) DOS for the 60-atom Bi_2Te_3 supercell doped with In, Po and Na, respectively, compared to undoped Bi_2Te_3. The reference for energy ($E = 0$ eV) corresponds to the VB maximum of undoped Bi_2Te_3. (d)-(f) Partial DOS for the In, Po, and Na (substituting ionic Te) atom, respectively; and (g)-(i) Partial DOS for the neighboring host atoms bonded to In, Po and Na, respectively.

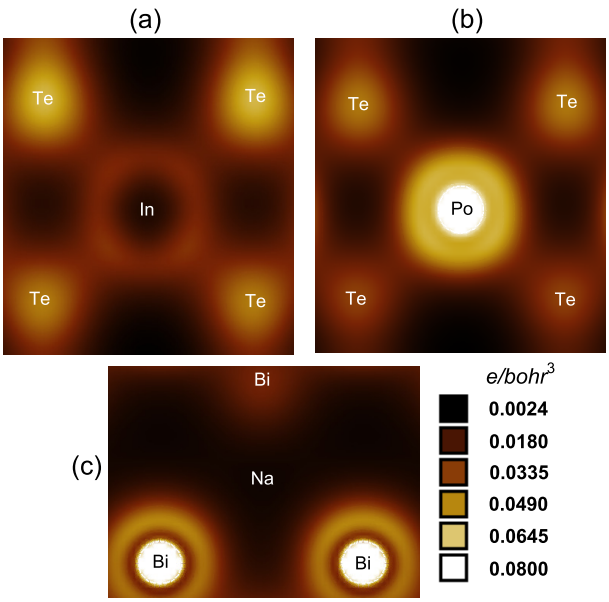

Figure 3.3: Electron charge density (in units of $e/bohr^3$) projected onto the x-z plane for Bi_2Te_3 doped with (a) In substituting a Bi atom, (b) Po substituting a Bi atom, and (c) Na substituting an ionic Te atom.

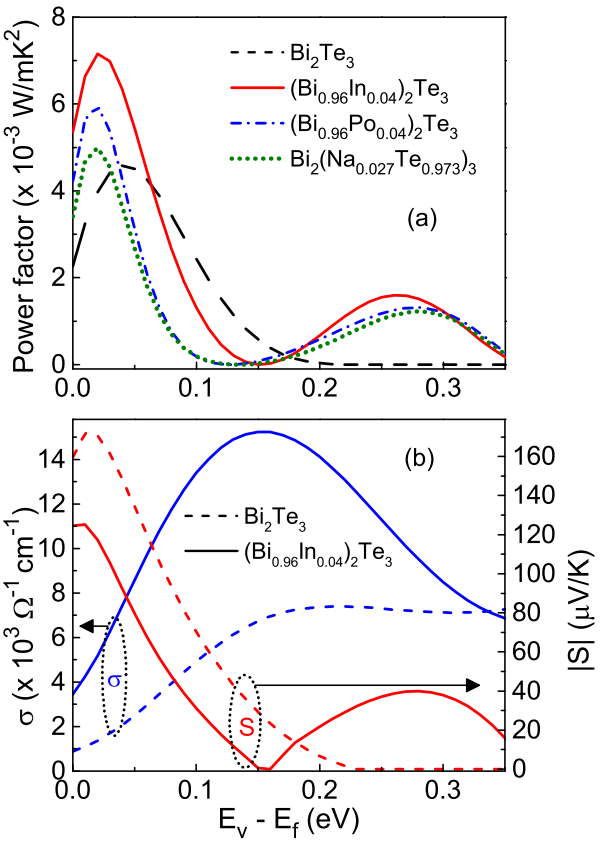

Figure 3.4: (a) Power factor versus Fermi energy for Bi_2Te_3 doped with In, Po and Na at T=300 K. (b) Conductivity and Seebeck coefficient versus Fermi energy for Bi_2Te_3 doped with In. The corresponding results for the undoped case are also shown for comparison.

Chapter 4

Tight binding modelling of in-plane and cross-plane transport in turbostratic MoS_2/WS_2 heterostructure

4.1 Introduction

Transition metal dichalcogenides (TMD) have gained a lot of interest in the recent years owing to their interesting electronic, optical and mechanical properties. Mo and W based chalcogenides are particularly relevant with their band gaps in the visible to near-infraed range. They find a variety of applications in field effect transistors(FET), tunneling devices, photodetectors, solar cells, hydrogen catalysis and sensors. [59, 60] In addition, the valley degree of freedom in TMDs can be exploited via circularly polarized light to design valleytronic devices. [61] The electrical and optical properties of the devices

can be tuned by changing number of layers of TMDs, application of strain and stacking TMD heterostructures. [62] For instance, the band gap changes from direct to indirect when moving from monolayer to few-layer MoS_2 and application of strain can cause a semiconductor to metal transition. [63, 64]

In this chapter, engineering of electronic properties of MoS_2/WS_2 heterostructure is studied. Vertical FETs using MoS_2/WS_2 heterostructure have been demonstrated with improved ON/OFF ratio and high photoresponsivity. [65] Ultrafast charge transfer in MoS_2/WS_2 heterostructure has been demonstrated making it a promising candidate for optoelectronics and light harvesting. [66] Fabrication of these heterostructures by mechanical transfer or sputtering with precision control is challenging. [67] The stacking orientation for the heterostructure cannot be controlled and the optoelectronic properties will thus be a function of the misorientation angle between the individual layers. Even if precision control can be obtained through techniques like vapour phase growth, it is instructive to study the change in electronic properties of MoS_2/WS_2 heterostructure with rotational degree of freedom. [68] In studying the turbostratic heterostructure, the number of atoms in a unit cell can increase to tens of thousands for small angles of misorientation as shown in Figure 4.1. In such a scenario, first principles approach becomes computationally demanding and an analytical approach such as tight binding (TB) needs to be adopted.

While the perfectly stacked MoS_2/WS_2 heterostructure has been investigated theoretically by first principles, there has been no study conducted on the turbostratic structure. [69] The TB models developed for TMDs have not been extended to the study of heterostrucures and this study aims to develop a generic TB model that can be easily extended to turbostratic sructures. [70, 71] First, the DFT bandstructure for the monolayer MoS_2 and WS_2 is calculated and the basis set for TB model is obtained by analyzing the

orbital nature of the bands near the high symmetry points. The TB parameters are then obtained by fitting to the DFT results. The TB model is then extended to the MoS_2/WS_2 heterostructure and the effect of misorientation on the in-plane electronic band structure is studied. Finally, cross-plane transport in turbostratic MoS_2/WS_2 heterostructure is analyzed by Green's function approach.

4.2 Tight binding model

The unit cell for monolayer MoS_2 and WS_2 has a triangular metal sublattice sandwiched between two triangular S sublattices, while the unit cell for bulk MoS_2 and WS_2 has a trigonal prismatic (2H) strucure with the S sublattice of one layer overlapping with the metal sublattice of the adjacent layer. The DFT calculations are carried out using QUANTUM ESPRESSO. Norm conserving LDA pseudopotential is used as parametrized by Perdew and Zunger. Energy cutoff of 60 Ry and k point grid of 18x18x1 is used. The optimized lattice constant, a for MoS_2 and WS_2 are 3.14 Å and 3.07 Å respectively. We focus first on the orbital composition of the bands near high symmetry points. As shown in Figure 4.2 and listed out in Table 4.1, for the monolayer MoS_2, the valence band maximum at K is composed primarily of $d_{x^2-y^2}$ and d_{xy} while the conduction band minimum is composed of $d_{3z^2-r^2}$. In bilayer MoS_2, the valence band maximum shifts to the Γ point, where the orbital character shifts from a dominant $d_{3z^2-r^2}$ in the case of monolayer to a mixture of $d_{3z^2-r^2}$ and p_z. A similar observation is made in the case of WS_2. Hence, the S p orbitals need to be considered in addition to the Mo/W d orbitals in order to fully describe the change in the band structure in bilayer or heterostructures from a direct to indirect band gap due to the contribution of S p_z orbital at the Γ point. The S p orbitals are also needed to accurately characterize the electronic state at the

Q point (midway between K-Γ), which becomes the conduction band edge in multilayer structures.

The TB model is first constructed for a monolayer structure and then extended to multilayer case. A nearest neighbour TB model employing the Slater-Koster approach is utilized. [14] Monolayer MS_2 has 11 atomic bases $|\phi_\mu\rangle$ consisting of 5 M (Mo/W) d orbitals $\{d_{3z^2-r^2}, d_{x^2-y^2}, d_{xy}, d_{xz}, d_{yz}\}$ and 3 p orbitals $\{p_x, p_y, p_z\}$ for the top and bottom S atoms. The basis orbitals $|\phi_\mu\rangle$ are assumed to be Löwdin orthogonalized orbitals, so as to eliminate the overlap matrix and minimize the number of fitting parameters. In constructing the TB hamiltonian, only the nearest neighbour interactions are considered, that is interactions between atoms at a distance greater than a are neglected. The matrix elements of the hamiltonian are given by

$$H_{\mu\mu'}(k) = \Delta_{\mu l}\delta(R_j - R_i)\delta(\mu - \mu') + \sum_{R_j} e^{ik.(R_i - R_j)} E_{\mu\mu'}(R_j - R_i) \tag{4.1}$$

Here, the term $\Delta_{\mu l}$ refers to the on-site crystal fields corresponding to atomic level l=0 ($d_{3z^2-r^2}$), l=1 (d_{xz}, d_{yz}), l=2 ($d_{x^2-y^2}, d_{xy}$) for the d orbitals and l=0 (p_z), l=1 (p_x, p_y) for the p orbitals. The second term in Eq. 4.1 represents the Bloch sum over all the nearest neigbouring atoms located at position R_j containing orbital $\phi_{\mu'}$ with respect to the atom at position R_i containing orbital ϕ_μ. The term $E_{\mu\mu'}(R_j - R_i)$ is the Slater-Koster energy integral, given by, $E_{\mu\mu'}(R_j - R_i) = \int \phi^*_\mu(r - R_i) H \phi_{\mu'}(r - R_j)$, which depends only on the direction cosines l, m, n of the vector $R_j - R_i$. The Slater-Koster enegy integrals are in turn written in terms of two-centre hopping parameters corresponding to the σ, π and δ bonds as described in Table 4.2.

There are 12 parameters in the TB model to be obtained by fitting to DFT band structure. Fitting is performed by minimizing the error between the TB and DFT results

as

$$Error = \sum_{CB,VB} \sum_{k} w(k)[E_{DFT}(k) - E_{TB}(k)]^2 \tag{4.2}$$

Only the lowest lying conduction band and valence band are considered for the fitting procedure. The weights, $w(k)$ are chosen so as to obtain a better fit at the high symmetry points, Γ, K and Q which are essential to describe the low energy transport. A genetic algorithm is used to optimize the parameters since the fitting needs to be done over a large parameter space. The vacuum level for monolayer MoS_2 and WS_2 is extracted from DFT calculations and aligned before fitting is performed. The TB parameters obtained for monolayer MoS_2 and WS_2 are reported in Table 4.3. The TB electronic band structure fit to the DFT data for monolayer MoS_2 and WS_2 is shown in Figure 4.3.

The hamiltonian for bilayer MoS_2 and WS_2 is obtained by keeping the same TB parameters from the monolayer case for intralayer hopping and adding additional terms for the interlayer hopping between the S ligands. The bilayer MS_2 has a total of 22 atomic basis and the distance between the S atoms of adjacent layers, w is 3.07Å and 2.97Å for MoS_2 and WS_2 respectively. The interlayer hopping parameters, $U_{pp\sigma}$ and $U_{pp\pi}$ are obtained by fitting to the bilayer DFT band structure at the Γ point. The fitted parameters are reported in Table 4.4 and the electronic band structure for bilayer MoS_2 and WS_2 is shown in Figure 4.4. As can be seen from the figure, addition of interlayer hopping between the p_z orbitals lifts the energy at Γ point, changing the band gap from direct one at K point in the monolayer system to an indirect band gap of Γ-K in the multilayer case.

The electronic bandstructure for MoS_2/WS_2 heterostructure is obtained in a similar manner to the bilayer structure. In the case of a heterostructure, there is the additional complexity introduced by induced strain due to lattice mismatch between the two layers.

In the case of MoS_2/WS_2 heterostructure, the lattice constant of WS_2 is set to that of MoS_2. The resulting lattice mismatch is minimum and the induced strain is 1.2%. But, for the sake of accuracy, we include the effect of this minimal strain in the TB model. The effects of strain is included in the TB model by the modulation of the two center parameter and in turn the Slater Koster energy integral, $E_{\mu\mu'}(R_j - R_i)$ with interatomic distance. A given strain profile, $\epsilon(x, y)$ changes the interatomic distance as, $(R_j - R_i) = [I + \epsilon(x, y)].(R_j^0 - R_i^0)$.The energy integral is then modified as,

$$E_{\mu\mu'}(R_j - R_i) = E_{\mu\mu'}(R_j^0 - R_i^0) \left(\frac{|R_j^0 - R_i^0|}{|R_j - R_i|} \right)^n \tag{4.3}$$

Here n is the empirical parameter obtained by fitting the direct band gap of MoS_2/WS_2 heterostructure at the K point to DFT results. The value of n is estimated to be 1.5. The hamiltonian for the MoS_2/WS_2 heterostructure is now constructed by including the effect of strain in WS_2 layer and fitting the interlayer hopping parameters to DFT data. The fitted parameters are given in Table 4.4 and the electronic band structure is shown in Figure 4.5. The band structure shows an indirect band gap Γ-K similar to the bilayer structures.

4.3 Transport in turbostratic MoS_2/WS_2 heterostructure

4.3.1 In-plane transport

With the TB parameters obtained and the model verified for MoS_2/WS_2 heterostructure, the electronic band structure for turbostratic MoS_2/WS_2 can now be obtained. One of the

first steps to be taken while studying misoriented structures is to find the commensurate unit cell. Following the procedure laid out in Ref. [72] for turbostratic graphene, integers p and q are chosen to lead to the desired rotation angle as given by

$$\theta = cos^{-1}\left(\frac{3q^2 - p^2}{3q^2 + p^2}\right) \tag{4.4}$$

The commensuration vectors, t_1 and t_2 are then specified by the following equations depending on the value of $\delta = 3/\text{gcd(p,3)}$. For the case of δ=1,

$$t_1 = \frac{1}{\gamma}\begin{pmatrix} p + 3q \\ -2p \end{pmatrix}, t_2 = \frac{1}{\gamma}\begin{pmatrix} 2p \\ -p + 3q \end{pmatrix} \tag{4.5}$$

and for the case of δ=3,

$$t_1 = \frac{1}{\gamma}\begin{pmatrix} -p - q \\ 2q \end{pmatrix}, t_2 = \frac{1}{\gamma}\begin{pmatrix} 2q \\ -p + q \end{pmatrix} \tag{4.6}$$

The total number of atoms in the turbostratic unit cell is given by, $N = \frac{18}{\delta\gamma^2}(3q^2 + p^2)$. For the case of lower bound of $N = (sin^2(\theta/2))^{-1}$, a new pattern called moiré pattern emerges and the moiré periodicity is given by, $D = \frac{a}{2sin(\theta/2)}$. Once the atomic positions for the turbostratic MoS_2/WS_2 heterostructure are obtained using the commensuration vectors, the hamiltonian elements can be obtained using Eq. 4.1. The total number of atomic basis will be equal to the number of atoms in the unit cell (N) multiplied by the number of orbitals per atom. The hamiltonian is constructed as described above for the perfectly aligned MoS_2/WS_2 heterostructure. The additional factor to consider for the turbostratic case is the change in the interlayer hopping parameters $U_{pp\sigma}$ and $U_{pp\pi}$ due

to change in the S-S interatomic distance between the MoS_2 and WS_2 layers. $U_{pp\sigma}$ and $U_{pp\pi}$ are scaled according to Eq. 4.3. The change in S-S bond angle is handled implicitly in the hamiltonian. The hamiltonian and band structure is obtained for various angles of rotation.

In-plane electronic band structure for turbostratic MoS_2/WS_2 heterostructure for rotation angles of 21.78° and 13.17° is shown in Figure 4.6. For comparison, band structure of perfectly aligned MoS_2/WS_2 heterostructure with the same supercell size as the turbostratic heterostructure is also plotted. The K valley in both the conduction band as well as the valence band remains invariant with respect to the rotation angle θ. This can be explained by the fact that the valence band K valley is completely localized to the d orbitals in the W layer of WS_2, while the conduction band K valley is completely localized to the d orbitals in the Mo layer of MoS_2. [62] Due to this, the change in S-S bonding between MoS_2 and WS_2 layers with rotation does not affect the K valley. On the other hand, the valence band energy at the Γ valley is very sensitive to θ. This can be attributed to the significant contribution of the S p orbitals to the energy of the valence band Γ valley for multilayer TMDs as seen in Table 4.1. With rotation of WS_2 layer with respect to MoS_2, the magnitude of the interlayer S-S hopping is modified, thereby changing the Γ valley energy. Figure 4.7 illustrates the change in energy at the valence band Γ valley as a function of rotation angle for turbostratic MoS_2/WS_2 heterostructure. Smaller interlayer S-S interatomic distance results in stronger interlayer S-S hopping. And the weakening of S-S hopping with θ lowers energy at Γ valley. Band gap increase of 80 meV is observed for $\theta = 21.78°$ as compared to the perfectly aligned heterostructure. The role of S-S hopping can also be illustrated by comparing bilayer MoS_2/WS_2 heterostructure with monolayer MoS_2/WS_2 heterostructure. Additional interlayer S-S hopping lifts valence band Γ energy in the bilayer heterostructure while simultaneously

lowering conduction band Q energy. Further analysis of impact of rotation on in-palne transport will require band unfolding.

4.3.2 Cross-plane transport

Cross-plane transport for turbostratic MoS_2/WS_2 heterostructure is analyzed through Green's function approach. The device is constructed by considering two layers of MoS_2 as left lead; one layer MoS_2/one layer WS_2 as conductor region and two layers of WS_2 as right lead as shown in Figure 4.8. The device hamiltonian can then be written as

$$H = \begin{bmatrix} H_{MoS_2} & H_{MoS_2-MoS_2/WS_2} & 0 \\ H^{\dagger}_{MoS_2-MoS_2/WS_2} & H_{MoS_2/WS_2} & H^{\dagger}_{WS_2-MoS_2/WS_2} \\ 0 & H_{WS_2-MoS_2/WS_2} & H_{WS_2} \end{bmatrix} \tag{4.7}$$

$6 \times 6 \times 1$ uniform k-grid is generated with eack k-point having equal weight. The device hamiltonian is calculated for each k-point according to Eq. 4.7. Green's function formalism yields the transmission function given by

$$T(E,k) = Tr[\Gamma_{MoS_2} G^{r}_{MoS_2/WS_2} [\Gamma_{WS_2} G^{a}_{MoS_2/WS_2}] \tag{4.8}$$

Here Γ_{MoS_2} and Γ_{WS_2} represent the coupling of the left lead and the right lead respectively with the conductor region, while $G^{r}_{MoS_2/WS_2}$ and $G^{a}_{MoS_2/WS_2}$ is the retarded and advanced device Green's function. The transmission function obtained from Eq. 4.8 is then integrated over k-space to yield transmission as a function of energy given by $T(E) = \sum_k T(E,k)$. Inter-layer resistance (R) is then obtained through Landauer formalism for different Fermi level values.

$$\frac{1}{R} = \frac{2e^2}{h} \int_0^\infty T(E) \left(-\frac{\partial f}{\partial E} \right) dE \ , \tag{4.9}$$

One of the things to consider is the effect of supercell size on the cross-plane transport properties. Large supercells cause band folding in the corresponding Brillouin zone and must be treated with care in the absence of band unfolding. To illustrate this, normalized k-resolved conductance is plotted in Figure 4.9 in the first brillouin zone for perfectly aligned MoS_2/WS_2 heterostructure of different supercell sizes. Figure 4.9 (a)-(c) correspond to hole transport with $E_F = E_V$, while Figure 4.9 (d)-(f) correspond to electron transport with $E_F = E_C$. It is to be noted that the size of brillouin zone decreases with increasing supercell size. Brillouin zones for the different supercells have been scaled to the same size for visualization purpose. For the case of $E_F = E_V$, it can be clearly seen that conductance is maximum at the Γ point for the smallest unit cell, which corresponds to the valence band maximum. As the supercell size is increased, conductance away from Γ also increases due to band folding increasing the density of states for k points away from Γ. Similarly for $E_F = E_C$, for the smallest unit cell, conductance is maximum at Q which is the conduction band minimum. Band folding into the smaller brillouin zone for larger supercells changes the conductance contour significantly. It is difficult to visualize the mapping of Q points from the larger brillouin zone to smaller brillouin zone to make a direct comparison. The conductance per unit area for the larger supercell will not recover the conductance per unit area for the smaller supercell. Hence, it is necessary to compare the carrier transport of a rotated supercell to unrotated supercell of same size.

Carrier transport across the turbostratic MoS_2/WS_2 heterostructure is now analyzed. Approximately 10% change in interfacial electrical resistance is observed for holes for rotation angles of 21.78° and 13.17° as seen in Figure 4.10(a). There is nearly no dependence

on the fermi level. The change in resistance is due to the change in interlayer S-S bond lengths of rotated MoS_2/WS_2 layers. This also affects the $E_K - E_\Gamma$ separation, but does not affect the transport because of the large Γ-K separation. The change in E_Γ in the rotated heterostructure affects cross-plane transport by changing valence band barrier height. Normalized conductance plotted in the first brillouin zone shown in Figure 4.11 shows that the hole transport in k-space is not significantly affected. Unlike hole transport, electron transport is not restricted to high symmetry points of Γ and K. Therefore, choice of tight binding parameters is a critical exercise, since a good fit away from the high symmetry points is essential to get accurate results. As seen in Figure 4.12, electron transport is impacted through mismatch in overlap in the momentum space. But these effects are averaged out with the electron conduction being affected only moderately (∼30%) as shown in Figure 4.10(b). Misorientation effect may be not as crucial in heterojunctions as in homogeneous turbostratic structures.

The current-voltage ($I-V$) characteristics are obtained next using the nonequilibrium Green's function (NEGF) approach. The diagonal elements of the left lead and the right lead are modified according to the voltage applied (V) as $H_{ij} = H_{ij} \pm \delta_{ij}(\frac{V}{2})$. The tunneling current is then obtained by

$$I = \frac{2e}{h} \int_0^\infty T(E)[f(E-\mu_R) - f(E-\mu_L)]dE \ , \tag{4.10}$$

Here, μ_R and μ_L refers to the chemical potentials of the right and left lead respectively which accounts for the applied voltage as well as the doping effects. Hole and electron tunneling current is calculated by setting Fermi level to valence band maximum and conduction band minimum respectively. From Figure 4.13(a), it can be seen that hole tunneling current for K valley is reduced compared to Γ valley. While hole tunneling

current is not affected by rotation significantly, electron tunneling current is reduced slightly as seen in Figure 4.12(b). The maximum reduction in electron tunneling current for rotation angle of 21.78° is 0.7.

4.4 Conclusion

In conclusion, a tight binding model has been developed to describe the electronic band structure of MoS_2/WS_2 heterostructure by fitting to DFT data. The model is then extended to turbostratic heterostructure and both in-plane as well as cross-plane transport is analyzed. In-plane transport is not significantly impacted with only minor changes to the electronic band structure. On the other hand, misorientation effect on cross-plane transport is moderately impacted with upto 10% change in the interfacial electrical resistance for holes and 30% for electrons. This is attributed to change in interlayer S-S bond length and additionally, reduced overlap in the momentum space for electrons. NEGF calculations show no change in hole tunneling current while electron tunneling current is slighly reduced with rotation angle.

Table 4.1: Orbital character of the bands at high symmetry points for monolayer and bilayer MoS_2 as obtained from DFT calculations.

Symmetry point	p_x	p_y	p_z	$d_{3z^2-r^2}$	$d_{x^2-y^2}$	d_{xy}	d_{xz}	d_{yz}	Other orbitals
Monolayer MoS_2 - Valence band									
Γ	0%	0%	34%	61%	0%	0%	0%	0%	5%
K	10%	10%	0%	0%	38%	38%	0%	0%	4%
Monolayer MoS_2 - Conduction band									
K	6%	6%	0%	79%	0%	0%	0%	0%	9%
Q	14%	14%	12%	8%	21%	21%	0%	0%	10%
Biayer MoS_2 - Valence band									
Γ	0%	0%	43%	49%	0%	0%	0%	0%	8%
K	10%	10%	0%	0%	38%	38%	0%	0%	4%
Bilayer MoS_2 - Conduction band									
K	6%	6%	0%	79%	0%	0%	0%	0%	9%
Q	14%	14%	11%	9%	20%	20%	2%	2%	8%

Table 4.2: Slater Koster energy integrals $E_{\mu\mu'}$. $E_{\mu\mu'}$ for integrals not expilicilty written can be found by cyclical permutation of μ, μ' and l, m, n. $E_{\mu'\mu} = (-1)^{p_1+p_2} E_{\mu\mu'}$ where p_1 and p_2 are the parities of orbitals μ and μ'.

E_{p_x,p_x}	$l^2V_{pp\sigma} + (1-l^2)V_{pp\pi}$
E_{p_x,p_y}	$lmV_{pp\sigma} - lmV_{pp\pi}$
$E_{d_{xy},d_{xy}}$	$3l^2m^2V_{dd\sigma} + (l^2+m^2-4l^2m^2)V_{dd\pi} + (n^2+l^2m^2)V_{dd\delta}$
$E_{d_{xy},d_{yz}}$	$3lm^2nV_{dd\sigma} + ln(1-4m^2)V_{dd\pi} + ln(m^2-1)V_{dd\delta}$
$E_{d_{xy},d_{x^2-y^2}}$	$\frac{3}{2}lm(l^2-m^2)V_{dd\sigma} + 2lm(m^2-l^2)V_{dd\pi} + \frac{1}{2}lm(l^2-m^2)V_{dd\delta}$
$E_{d_{yz},d_{x^2-y^2}}$	$\frac{3}{2}mn(l^2-m^2)V_{dd\sigma} - mn[1+2(l^2-m^2)]V_{dd\pi} + mn[1+\frac{1}{2}(l^2-m^2)]V_{dd\delta}$
$E_{d_{zx},d_{x^2-y^2}}$	$\frac{3}{2}nl(l^2-m^2)V_{dd\sigma} + nl[1-2(l^2-m^2)]V_{dd\pi} - nl[1-\frac{1}{2}(l^2-m^2)]V_{dd\delta}$
$E_{d_{xy},d_{3z^2-r^2}}$	$\sqrt{3}lm[n^2-\frac{1}{2}(l^2+m^2)]V_{dd\sigma} - 2\sqrt{3}lmn^2V_{dd\pi} + \frac{1}{2}\sqrt{3}lm(1+n^2)V_{dd\delta}$
$E_{d_{yz},d_{3z^2-r^2}}$	$\sqrt{3}mn[n^2-\frac{1}{2}(l^2+m^2)]V_{dd\sigma} + \sqrt{3}mn(l^2+m^2-n^2)V_{dd\pi} - \frac{\sqrt{3}}{2}mn(l^2+m^2)V_{dd\delta}$
$E_{d_{zx},d_{3z^2-r^2}}$	$\sqrt{3}ln[n^2-\frac{1}{2}(l^2+m^2)]V_{dd\sigma} + \sqrt{3}ln(l^2+m^2-n^2)V_{dd\pi} - \frac{\sqrt{3}}{2}ln(l^2+m^2)V_{dd\delta}$
$E_{d_{x^2-y^2},d_{x^2-y^2}}$	$\frac{3}{4}(l^2-m^2)^2V_{dd\sigma} + [l^2+m^2-(l^2-m^2)^2]V_{dd\pi} + [n^2+\frac{1}{4}(l^2-m^2)^2]V_{dd\delta}$
$E_{d_{3z^2-r^2},d_{3z^2-r^2}}$	$[n^2-\frac{1}{2}(l^2+m^2)]^2V_{dd\sigma} + 3n^2(l^2+m^2)V_{dd\pi} + \frac{3}{4}(l^2+m^2)^2V_{dd\delta}$
$E_{d_{x^2-y^2},d_{3z^2-r^2}}$	$\frac{\sqrt{3}}{2}(l^2-m^2)[n^2-\frac{1}{2}(l^2+m^2)]V_{dd\sigma} + \sqrt{3}n^2(m^2-l^2)V_{dd\pi} + \frac{\sqrt{3}}{4}(1+n^2)(l^2-m^2)V_{dd\delta}$
$E_{p_x,d_{xy}}$	$\sqrt{3}l^2mV_{pd\sigma} + m(1-2l^2)V_{pd\pi}$
$E_{p_x,d_{yz}}$	$\sqrt{3}lmnV_{pd\sigma} - 2lmnV_{pd\pi}$
$E_{p_x,d_{zx}}$	$\sqrt{3}l^2nV_{pd\sigma} + n(1-2l^2)V_{pd\pi}$
$E_{p_x,d_{x^2-y^2}}$	$\frac{\sqrt{3}}{2}l(l^2-m^2)V_{pd\sigma} + l(1-l^2+m^2)V_{pd\pi}$
$E_{p_y,d_{x^2-y^2}}$	$\frac{\sqrt{3}}{2}m(l^2-m^2)V_{pd\sigma} - m(1+l^2-m^2)V_{pd\pi}$
$E_{p_z,d_{x^2-y^2}}$	$\frac{\sqrt{3}}{2}n(l^2-m^2)V_{pd\sigma} - n(l^2-m^2)V_{pd\pi}$
$E_{p_x,d_{3z^2-r^2}}$	$l[n^2-\frac{1}{2}(l^2+m^2)]V_{pd\sigma} - \sqrt{3}ln^2V_{pd\pi}$
$E_{p_y,d_{3z^2-r^2}}$	$m[n^2-\frac{1}{2}(l^2+m^2)]V_{pd\sigma} - \sqrt{3}mn^2V_{pd\pi}$
$E_{p_z,d_{3z^2-r^2}}$	$n[n^2-\frac{1}{2}(l^2+m^2)]V_{pd\sigma} + \sqrt{3}n(l^2+m^2)V_{pd\pi}$

Table 4.3: Two-center Slater-Koster tight binding parmeters obtained for monolayer MoS_2 and WS_2 in units of eV.

	MoS_2	WS_2
$V_{pp\sigma}$	-0.037	0.015
$V_{pp\pi}$	-0.13	-0.126
$V_{dd\sigma}$	-3.467	-4.006
$V_{dd\pi}$	4.957	4.263
$V_{dd\delta}$	-1.0	-0.538
$V_{pd\sigma}$	8.457	7.565
$V_{pd\pi}$	0.245	0.096
Δ_{p0}	-4.073	-4.168
Δ_{p1}	-2.857	-2.493
Δ_{d0}	-11.378	-9.598
Δ_{d1}	3.335	-0.115
Δ_{d2}	-13.803	-8.92

Table 4.4: Slater-Koster interlayer tight binding parmeters obtained for bilayer MoS_2, WS_2 and MoS_2/WS_2 heterostructure in units of eV.

	$U_{pp\sigma}$	$U_{pp\pi}$
MoS_2	0.437	-0.055
WS_2	-0.393	0.067
MoS_2/WS_2	-0.457	-0.0197

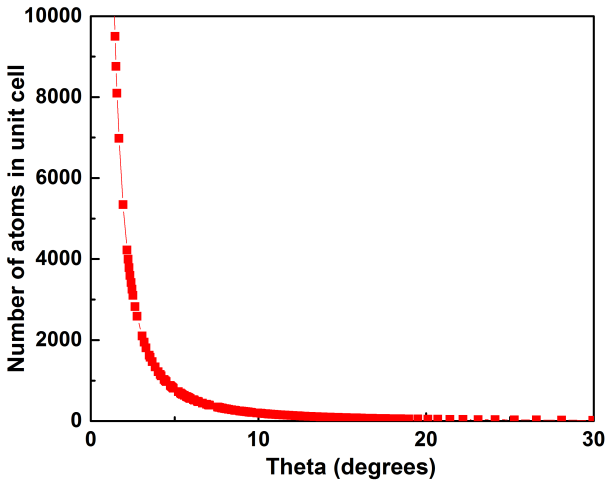

Figure 4.1: The minimum number of atoms in a turbostratic MoS_2/WS_2 heterostructure unit cell as a function of angle of rotation.

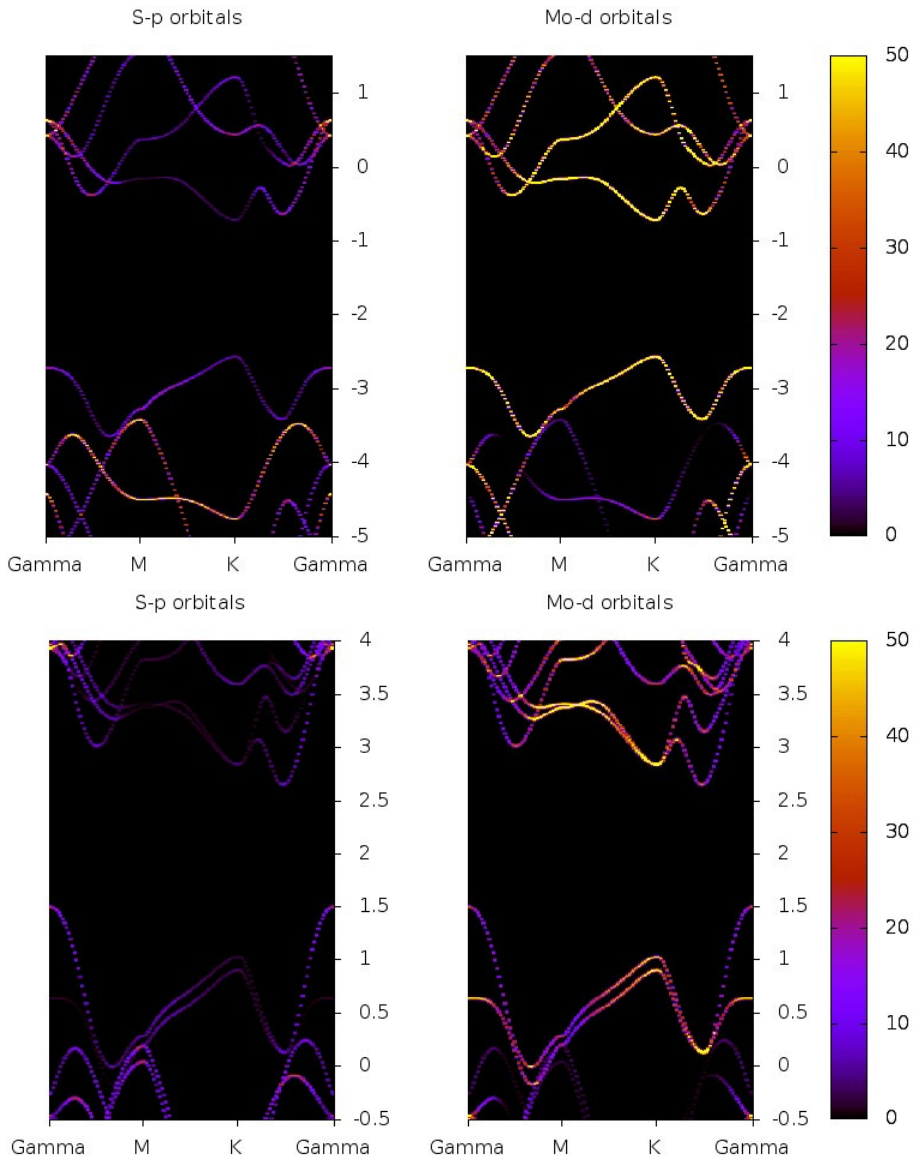

Figure 4.2: Projected bandstructure for (a) Monolayer MoS_2 and (b) Bilayer MoS_2.

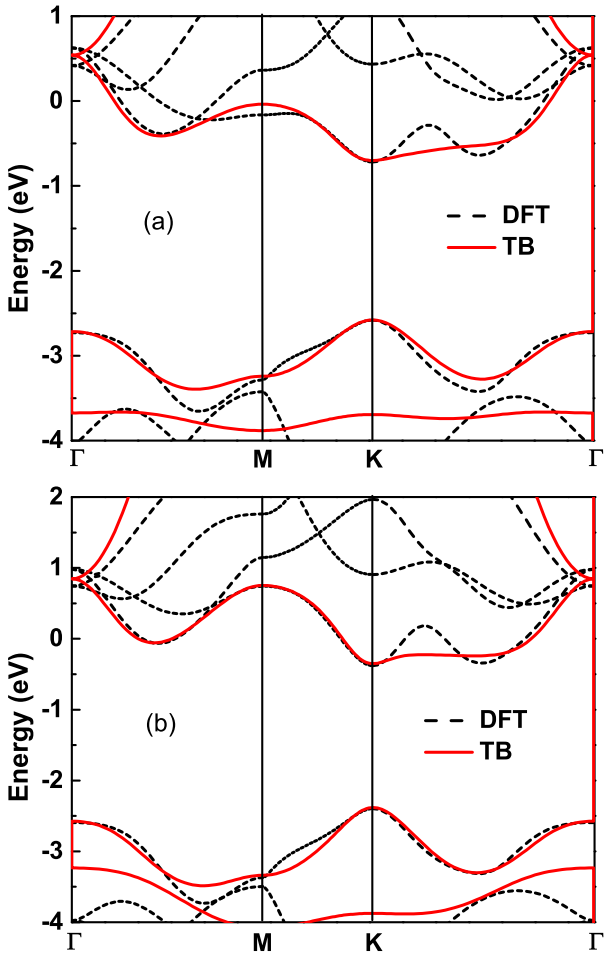

Figure 4.3: Electronic bandstructure of (a) Monolayer MoS_2 and (b) Monolayer WS_2.

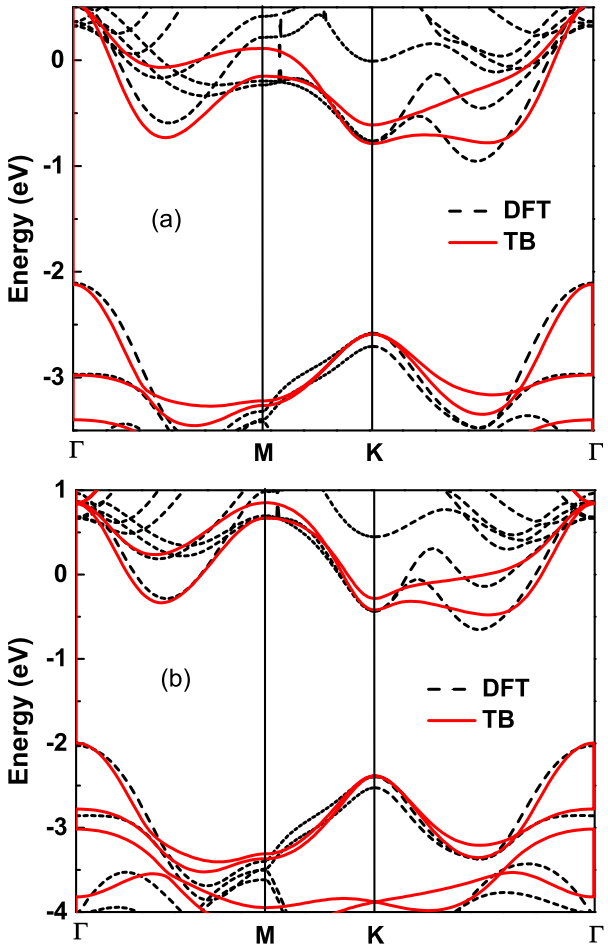

Figure 4.4: Electronic bandstructure of (a) Bilayer MoS_2 and (b) Bilayer WS_2.

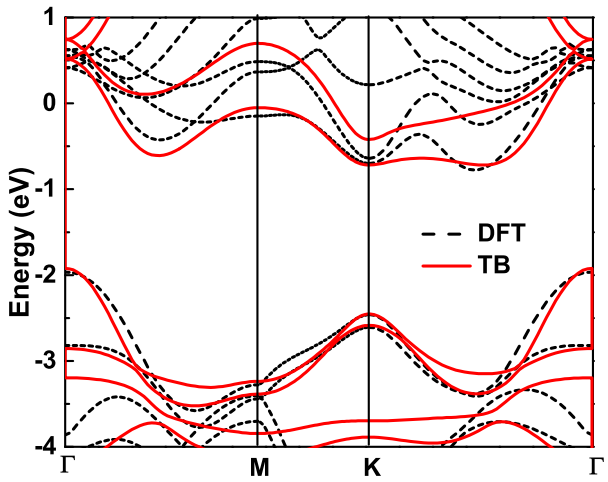

Figure 4.5: Electronic bandstructure of MoS_2/WS_2 heterostructure.

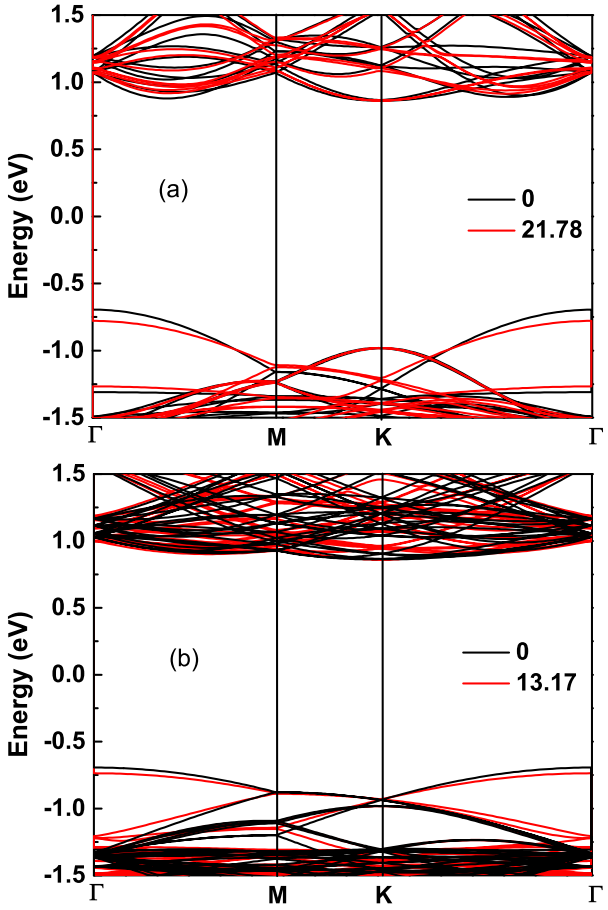

Figure 4.6: Electronic bandstructure of turbostratic MoS_2/WS_2 heterostructure for rotation angle of (a) 21.78° and (b) 13.17°.

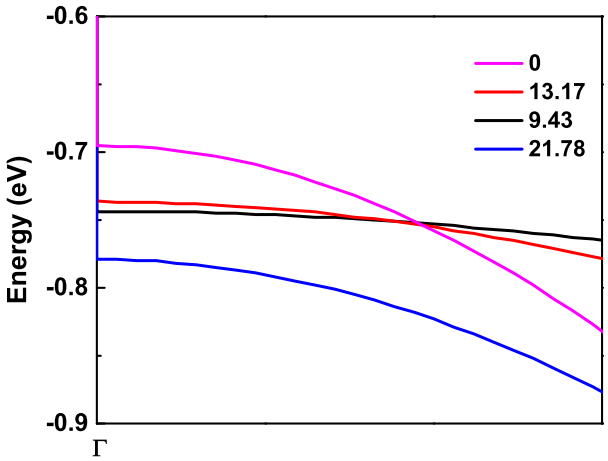

Figure 4.7: Energy at the valence band Γ valley as a function of rotation angle for turbostratic MoS_2/WS_2 heterostructure.

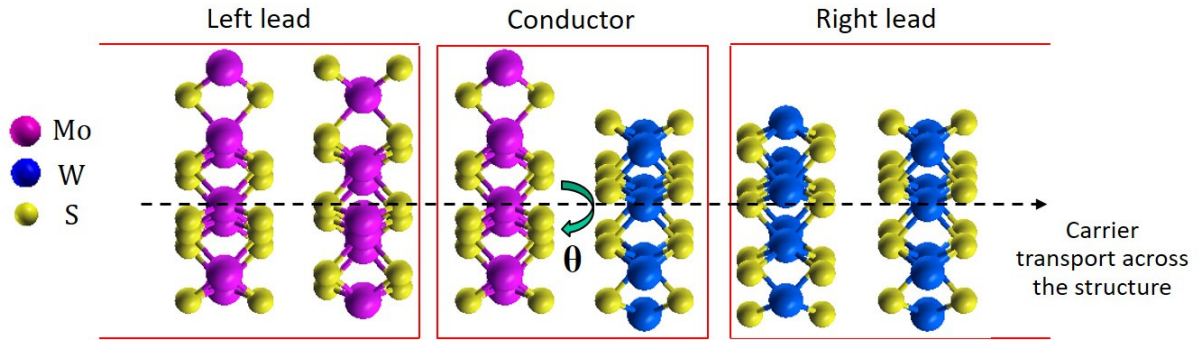

Figure 4.8: Schematic of the turbostratic MoS_2/WS_2 heterostructure device used for Green's function calculation.

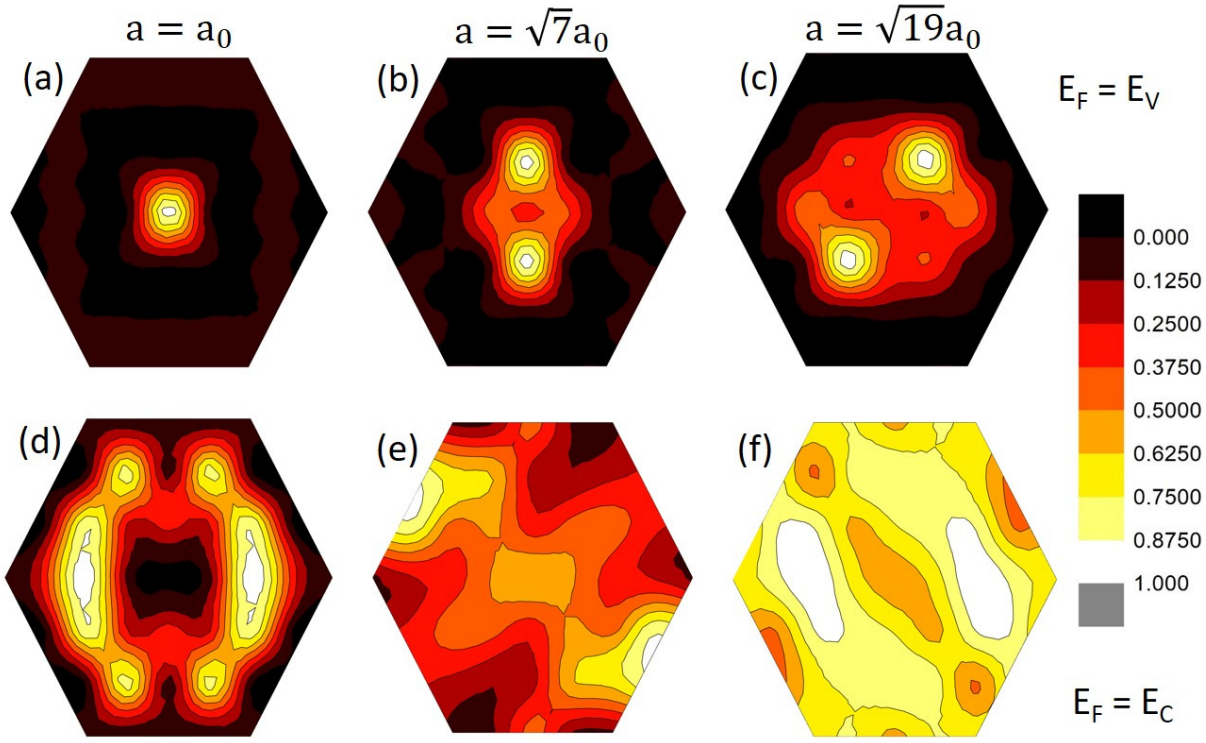

Figure 4.9: k-resolved normalized conductance for perfectly aligned MoS_2/WS_2 heterostructure of different supercell sizes for (a)-(c) E_F=E_V and (d)-(f) E_F=E_C.

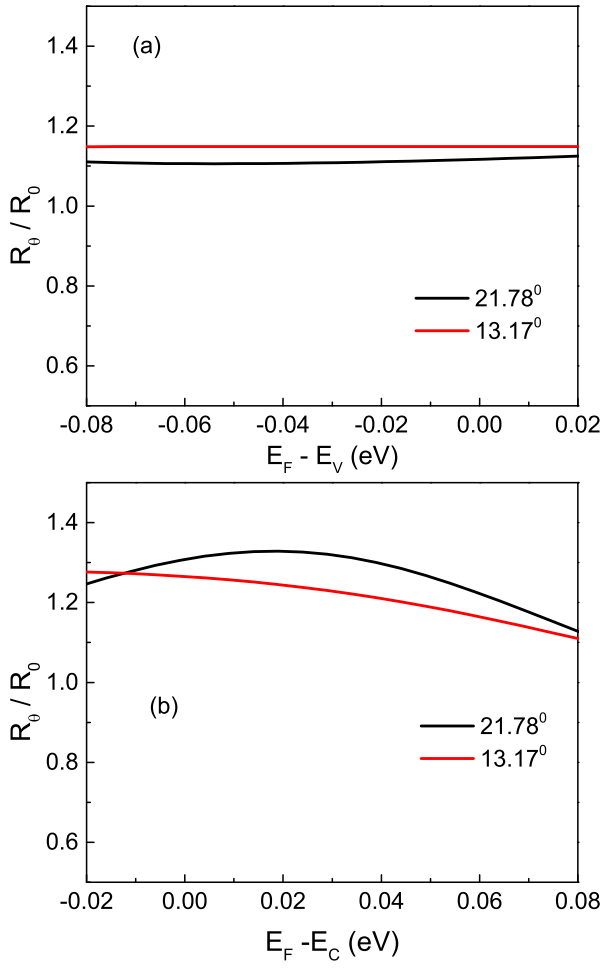

Figure 4.10: Interfacial electrical resistance for turbostratic MoS_2/WS_2 heterostructure as compared to the perfectly aligned heterostructure as a function of Fermi energy for (a) holes and (b) electrons.

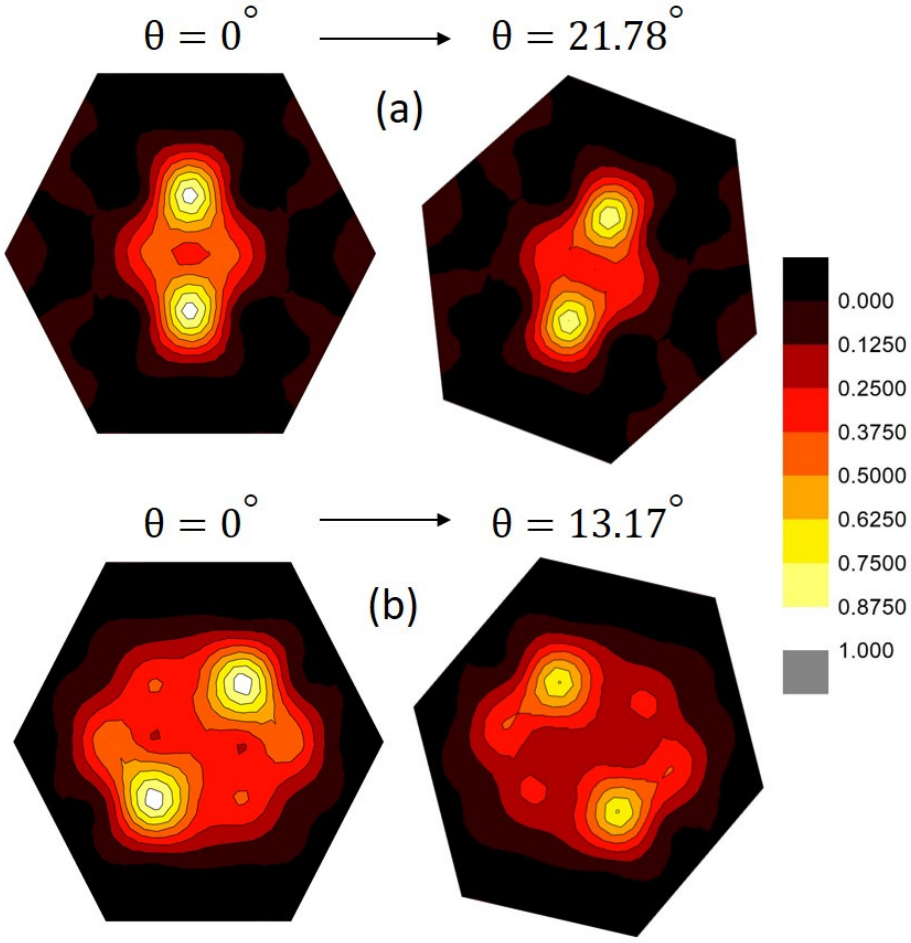

Figure 4.11: k-resolved normalized conductance for holes (E_F=E_V) in turbostratic MoS_2/WS_2 heterostructure compared to the perfectly aligned heterostructure of same supercell size for rotation angles of (a) 21.78° and (b) 13.17°.

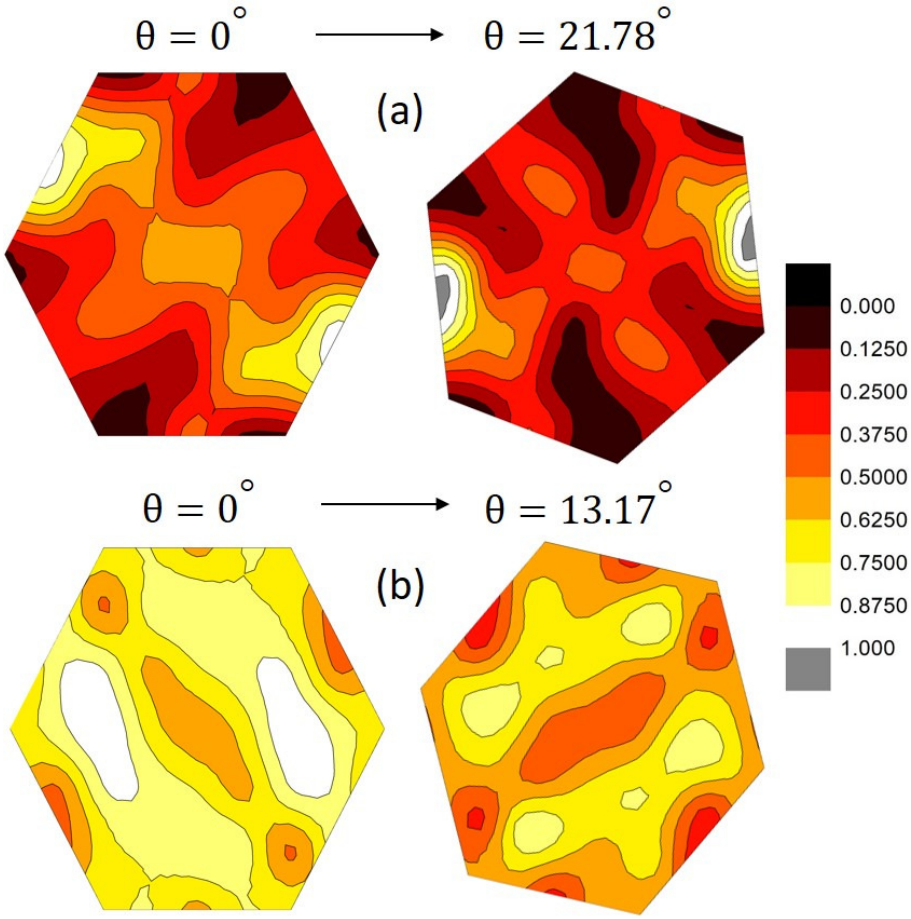

Figure 4.12: k-resolved normalized conductance for electrons (E_F=E_C) in turbostratic MoS_2/WS_2 heterostructure compared to the perfectly aligned heterostructure of same supercell size for rotation angles of (a) 21.78° and (b) 13.17°.

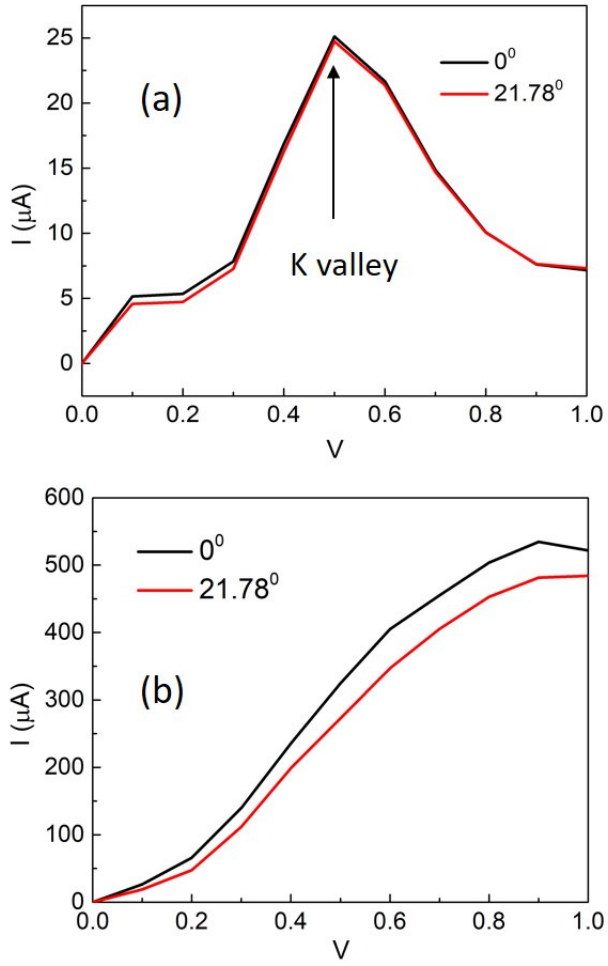

Figure 4.13: Current through turbostratic MoS_2/WS_2 heterostructure as a function of bias voltage for (a) holes and (b) electrons.

Chapter 5

Diamond/c-BN HEMTs for power applications: A theoretical feasibility analysis

5.1 Introduction

The current state-of-the-art power devices based on 4H-SiC and GaN have certain limitations due to their intrinsic material properties [73]. Diamond is a promising alternative as evidenced by the favorable figures of merit [74]. This is a result of the superior material properties exhibited by diamond such as band gap (5.45 eV), critical field ($\sim$10 MV/cm), mobility (4500 $cm^2/V{\cdot}s$ for electrons and 3800 $cm^2/V{\cdot}s$ for holes) and thermal conductivity (20 W/cm·K) [74]. The theoretical predictions also indicate that the lower limit of the specific on-resistance (R_{on}) is about two orders of magnitude smaller for diamond than GaN as can seen from Figure 5.1. The resulting improvements in device size and power density make diamond ideal for high-power, high-frequency, and

high-temperature applications. But, the promise of diamond power devices has not been fulfilled yet. Experimentally there have been material challenges such as the lack of high-quality, large-area crystalline diamond films. In addition, the large activation energy for n-type dopants (e.g., ∼0.6 eV for phosphorous) [75] has restricted the available diamond power devices to only p-type [76] due to the negligible free electron density.

However, recent advances in non-equilibrium growth and doping control may overcome the technical challenges that have long plagued this ultra-wide bandgap semiconductor. It was found that amorphous carbon films can be converted directly into diamond at ambient temperatures and pressures through nanosecond laser melting in a super undercooled state and subsequent rapid quenching [77]. By providing an epitaxial template such as sapphire or silicon, diamond grows from the liquid phase into a large-area single-crystal film via domain matching epitaxy. Furthermore, these films can be doped with p- and n-type dopants through alloying before the melting stage. During the rapid quenching process from the liquid phase, dopant concentrations can far exceed thermodynamic solubility limits through the solute trapping phenomenon [78]. Once the single-crystal film is formed, it is also possible to stack additional layers of epitaxial diamond and/or cubic boron nitride (c-BN, a closely lattice match material with a gap of 6.4 eV) through pulsed laser ablation with selected dopant types and concentrations. Accordingly, fabrication of multi-layer vertical homo- and hetero-junction structures is clearly within reach. Indeed, the synthesis of undoped diamond on c-BN has already been achieved [79].

These developments open up a particularly interesting prospect of modulation doping that can circumvent the issue of large donor activation energy and subsequent carrier mobility degradation, particularly in n-type devices [80]. If a type-I band offset can be formed at the diamond/c-BN interface, it is possible to dope the c-BN barrier while the undoped diamond layer can function as an efficient carrier channel with both high carrier

density and mobility (i.e., HEMTs). The aim of the present study is to examine, via a theoretical analysis, the feasibility of the diamond/c-BN based HEMTs and gauge their potential performance.

5.2 Results and discussion

5.2.1 DFT band offset

As it is well known, the 2D electron gas formed in a HEMT is highly dependent on the band alignment at the heterointerface. So far, theoretical calculations in the diamond/c-BN system have predicted two widely different values of 1.42 eV [81] and 0.71 eV [82] for the valence band offset (ΔE_V) for the (110) interface, while no experimental measurement is available. Hence, we estimate the corresponding values for the (111) oriented structure (grown on, for instance, C-sapphire) based on the first-principles density functional theory (DFT) approach. Specifically, the DFT calculations are carried out using norm conserving pseudopotentials with the generalized gradient approximation of Perdew-Zunger, as implemented in the plane wave based QUANTUM ESPRESSO package [28]. The (111) diamond/c-BN supercell is constructed with 6 layers of C and 6 layers of BN, and by setting the lattice constant of the supercell to the optimized lattice constant of diamond (3.54 Å). The supercell is fully relaxed until the total energy is minimized and the total force on the atoms is less than 10^{-4} Ry. In addition, of the various interface atomic configurations possible, the one leading to minimal energy is selected for which ΔE_V is calculated as [83]

$$\Delta E_V = (E_V^{\text{Diamond}} - E_V^{\text{c-BN}})_{\text{bulk}} + \Delta V. \tag{5.1}$$

The conduction band offset ΔE_C can then be evaluated by subtracting ΔE_V from the experimental band gap values. The first two terms in Eq. 5.1 refers to the difference in the valence band maximum energy between diamond and c-BN obtained from their respective bulk unit cells. This value is calculated to be 1.4 eV. The third term, ΔV accounts for the difference in the reference energy in the bulk calculation in addition to the dipolar correction at the interface. It is obtained by calculating the macroscopic average potential across the diamond/c-BN supercell as shown in Figure 5.2. After careful periodic averaging of the potential, ΔV is estimated to be approximately -0.9 eV to -1 eV. Thus, both ΔE_V and ΔE_C arrive at a similar value of around $0.4 - 0.5$ eV with a type-I alignment of the heterojunction. In the rest of the analysis, a conservative value of $\Delta E_C = 0.4$ eV is adopted for device characterization.

5.2.2 Device characteristics

Figure 5.3 shows the schematic of the prototype diamond/c-BN n-HEMT structure under investigation. In addition to the substrate (i.e., the epitaxial template mentioned above), the structure consists of n-diamond layer, undoped diamond channel, undoped c-BN spacer, and n-doped c-BN barrier layer. The doped c-BN barrier can be followed by an undoped dielectric to prevent surface conduction or other potential degradation. In c-BN, a doping level of 10^{18} cm^{-3} is assumed with an activation energy of 0.24 eV. The latter corresponds to the generally accepted ionization energy of Si dopants although a much smaller value of 0.05 eV is also reported in the literature [84]. Another option is carbon, whose activation energy was measured to be around 0.2 eV at a high dose [79]. The details of doping in the diamond layer is unimportant due to the low ionization efficiency (e.g., phosphorous with 0.6 eV). As for the gate, a Schottky contact is consid-

ered with a barrier height of 0.5 eV while the source and drain electrodes are assumed to be ideal ohmic contacts. Room temperature is considered throughout the study. The conduction band profile is obtained by using a Poisson simulator that takes into account the incomplete ionization model [Figure 5.4]. The resulting electron density distribution clearly shows the formation of a 2D electron channel in the diamond layer with the carrier concentrations exceeding 10^{18} cm^{-3} (at no gate bias). The modulation of the sheet charge density (n_s) with a gate voltage (V_{gs}) is illustrated in Figure 5.5 with the drain voltage (V_{ds}) set to 0 V. The maximum sheet carrier concentration obtained is 5×10^{12} cm^{-2}, which can be optimized further by varying the device parameters.

With the proof of concept for the diamond/c-BN HEMT established, the dc current characteristics are now determined by adopting an analytical charge control model [85]. The HEMT operation can be divided into two regimes; i.e., the linear and the velocity saturation regimes. In the linear regime, assuming total depletion in the c-BN barrier region [as the donor levels are located higher than the diamond conduction band edge as shown in Figure 5.4], the solution of the 1D Poisson's equation yields the sheet carrier density as

$$n_s(x) = \frac{\epsilon_{\mathrm{c-BN}}}{q(d + d_{\mathrm{2D}})}[V_{gs} - V_{th} - V_{ch}(x)], \tag{5.2}$$

where $\epsilon_{\mathrm{c-BN}}$ is the permittivity of c-BN, d the total thickness of the c-BN region, d_{2D} the 2D electron gas thickness, V_{th} the calculated threshold voltage, and V_{ch} the channel voltage resulting from the applied V_{ds}. The drain-source current, I_{ds} can then be obtained from the current density equation as

$$I_{ds} = wq\frac{\mu_0 \frac{dV_{ch}(x)}{dx}}{1 + \frac{1}{E_{cr}}\frac{dV_{ch}(x)}{dx}} n_s(x). \tag{5.3}$$

Here, w is the gate width, q the unit charge, μ_0 the low-field electron mobility (4500 $\mathrm{cm}^2/\mathrm{V}\cdot\mathrm{s}$), and E_{cr} the critical field for velocity saturation (10 kV/cm) in diamond [74]. As given, the model accounts for mobility degradation at high fields. The final expression for I_{ds} can be obtained by substituting Eq. 5.2 in Eq. 5.3 and then integrating Eq. 5.3 along the channel length by applying appropriate boundary conditions for the channel potential, in which the source and drain parasitic resistances can be taken into consideration. In the saturation regime, the channel can be divided into two regions, a low-field region and a high-field region near the drain end of the channel where the channel is pinched off. Using Eq. 5.3, the low-field channel length and the electric field in the corresponding region can be obtained. In the high-field region, the solution to 2D Poisson's equation yields an expression for the channel potential, $V_{ch}(x)$. I_{ds} is obtained by enforcing the current and field continuity between the two regions. The final expressions for I_{ds} can be found in Ref. [86].

The simulated $I-V$ characteristics are provided in Figure 5.6 for different gate biases. A maximum I_{ds} over 10 A/cm can be obtained which is comparable to GaN/AlGaN HEMTs. R_{on} extracted from the slope of the I_{ds}-V_{ds} curve in the linear region indicates a very low value ($0.05\ \mathrm{m\Omega}\cdot\mathrm{cm}^2$) in concert with the estimate shown in Figure 5.1. The calculated peak transconductance g_m is also large at 580 mS/mm. Both R_{on} and g_m are evaluated for $V_{gs} = 2$ V. Further, the unity gain cutoff frequency (f_T) is estimated by using parasitic gate capacitances as $f_T = \frac{g_m}{2\pi(C_{gs}+C_{gd})}$. Here, C_{gs} and C_{gd} are the gate-to-source and gate-to-drain capacitances, respectively, derived from the total charge Q_{sat} in the channel in the velocity saturation regime as $C_{g(d)s} = \frac{\partial Q_{\mathrm{sat}}}{\partial V_{g(d)s}}$. The result suggests f_T nearly in the sub-mm wave range (280 GHz).

5.3 Summary

In summary, a diamond/c-BN HEMT structure is proposed and evaluated. The analysis clearly predicts a highly promising performance in key aspects including I_{ds}, R_{on}, g_m, and f_T. With further optimization, it is anticipated that this device can provide a major advance in the high-power, high-frequency, high-temperature electronic applications.

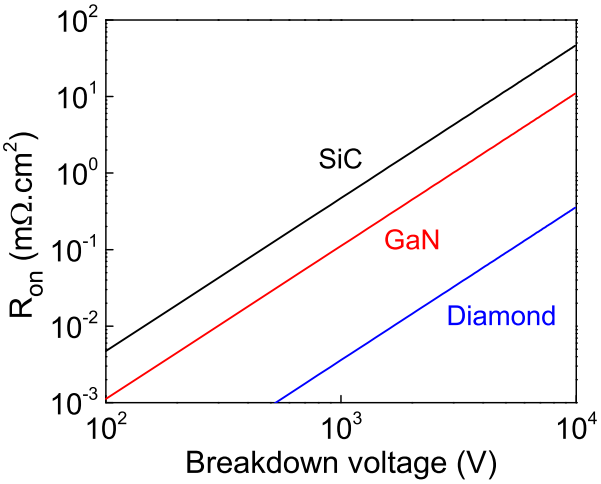

Figure 5.1: Theoretical specific on-resistance versus breakdown voltage for diamond in comparison with 4H-SiC and GaN.

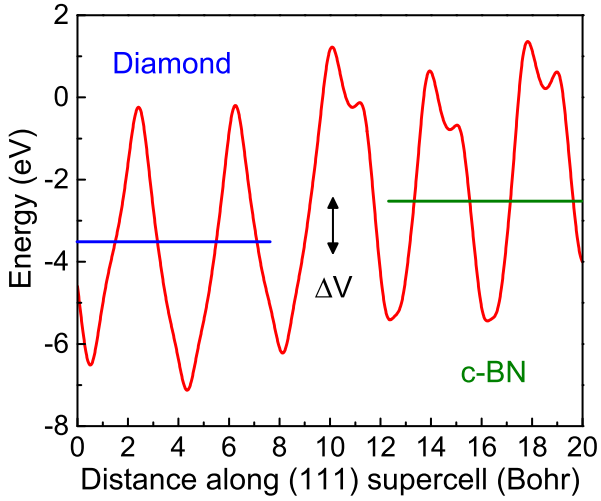

Figure 5.2: Planar averaged potential across the (111) diamond/c-BN heterostructure obtained from a DFT calculation.

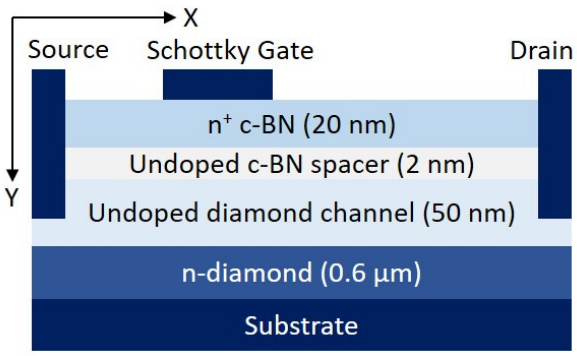

Figure 5.3: Schematic of the proposed diamond/c-BN HEMT prototype. The gate length is 1 μm, while the gate-to-source and gate-to-drain lengths are 1 μm and 2 μm, respectively.

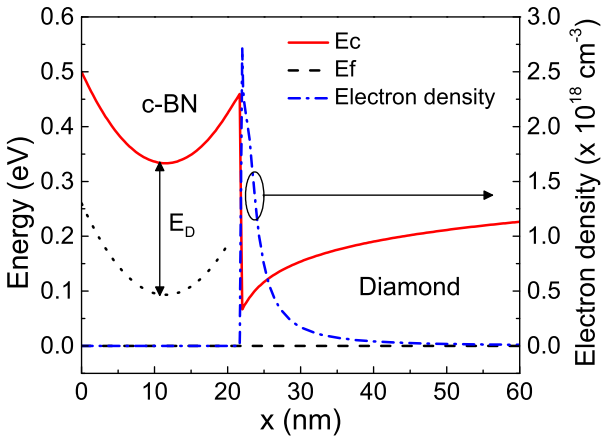

Figure 5.4: Calculated conduction band profile and the corresponding electron density in the channel with no gate bias. The activation energy (E_D) for the n-type dopants is also indicated in the c-BN layer.

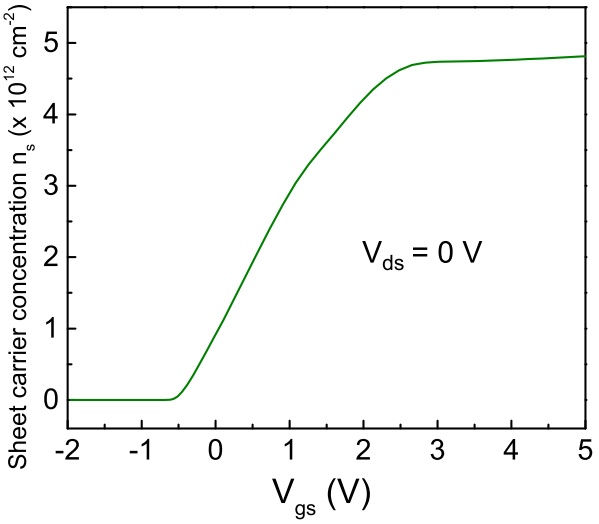

Figure 5.5: Sheet carrier density as a function of V_{gs} with V_{ds} set to 0 V.

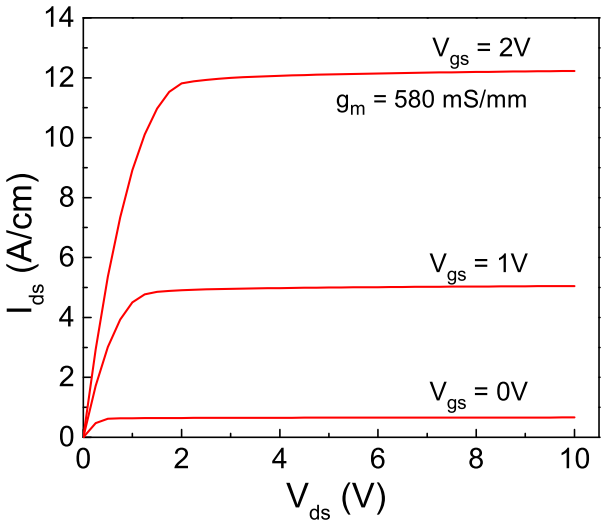

Figure 5.6: Output $I_{ds} - V_{ds}$ characteristics obtained at different V_{gs}. The transconductance g_m is estimated at $V_{gs} = 2$ V.

Chapter 6

Summary and outlook

6.1 Summary

As device sizes are shrinking and novel transistor device designs with heterostructures are being explored, semi-classical treatment of electron/phonon transport is no longer sufficient. Multiscale methodology is essential in these scenarios to be able to capture the quantum mechanical atomistic details while enabling the simulation of micro-scale structures at the same time. This ranges from using ab initio DFT for atomistic calculations to solving BTE for macroscopic transport simulation. In this thesis, multiscale modelling has been applied to study carrier transport in thermoelectrics, turbostratic 2D MoS_2/WS_2 heterostructure and diamond/c-BN high mobility electron transistor (HEMT).

The multiscale methodology was first applied to maximize the efficiency in thermoelectric materials, in particular, Bi_2Te_3. Our calculation illustrates the possibility of power factor enhancement in the Bi_2Te_3/Sb_2Te_3 heterostructure through effective energy filtering at the potential barrier. As the observed effect is spatially transient, the heterolayer dimension must remain much smaller than the carrier energy relaxation length.

In the case of p-type Bi_2Te_3, this characteristic length is estimated to be approximately 140 nm at room temperature which is clearly practicable. A similar but less pronounced increase is also obtained in the thermal resistance due to the additional phonon scattering at the interface. By combining the respective improvements in the power factor and the thermal resistance, it is not unreasonable to anticipate a significant enhancement in zT with an optimized geometry. The methodology used in the present analysis can be extended to other related material systems.

We next studied the the possibilty of increasing the power factor in bulk Bi_2Te_3 through resonant doping. Our DFT study identifies Po as the dopant that can potentially realize the desired resonant peak in the DOS of n-type Bi_2Te_3 while pinpointing In, Po, and Na for the p-type. The analysis clearly illustrates that these peaks originate from the impurity states of the dopant atom and its interaction with the host atoms. Transport calculations indeed predict the anticipated increase in the power factor that is directly attributed to the resonant features in the DOS. An investigation with a much lower doping concentration for In, Po and Na will help to quantify the precise enhancement in the power factor.

Our next area of study is impact of misorientation on electronic properties in MoS_2/WS_2 heterostructure. A tight binding model has been developed to describe the electronic band structure of MoS_2/WS_2 heterostructure by fitting to DFT data. The model is then extended to turbostratic heterostructure and both in-plane as well as cross-plane transport is analyzed. In-plane transport is not significantly impacted with only minor changes to the electronic band structure. On the other hand, misorientation effect on cross-plane transport is moderately impacted with upto 10% change in the interfacial electrical resistance for holes and 30% for electrons. This is attributed to change in interlayer S-S bond length and additionally, reduced overlap in the momentum space for

electrons. NEGF calculations show no change in hole tunneling current while electron tunneling current is slighly reduced with rotation angle.

Finally, a diamond/c-BN HEMT structure is proposed and evaluated. The analysis clearly predicts a highly promising performance in key aspects including I_{ds}, R_{on}, g_m, and f_T. With further optimization, it is anticipated that this device can provide a major advance in the high-power, high-frequency, high-temperature electronic applications.

6.2 Outlook

Phosphorene is another newly emerging 2D material gaining interest. Phosphorene has highly anisotropic transport properties. [87] Electrical conductivity is maximum along the armchair direction, while thermal conductivity is maximum along the zigzag direction. Therefore, phosphorene holds promise as a thermoelectric material. Phosphorene has maximum zT along armchair direction with value of 1.5 at room temperature. Phosphorene has a direct band gap at Γ. The band gap for bilayer phosphorene can vary between 0.78 eV- 1.04 eV depending on the stacking orientation. It would be an interesting problem to study the effect of misorientation of phosphorene layers on electronic and thermal transport and hence zT. Since both valence band maximum and conduction band minimum is at Γ, rotation will not affect the overlap in momentum space, and hence should not affect electron/hole transport significantly. On the other hand, interfacial thermal resistance can increase for certain angles of rotation as has been shown for turbostratic graphene. [88] With electron transport remaining unaffected and thermal conductivity potentially reducing, there is a possibility for increase in zT with misoriented phosphorene layers. The tight binding model developed for turbostratic MoS_2/WS_2 heterostructure in this thesis can be extended to the phosphorene system to study elec-

tronic transport properties in conjunction with NEGF. A similar approach can be used to study the thermal transport properties as well.

The diamond/c-BN HEMT proposed in this thesis can be further analyzed for dc and rf properties. Since the potential applications are in the high power- high frequency region, power-frequency analysis is needed. In addition, breakdown voltage calculation will also be necessary. The current simulation assumes ideal ohmic contacts due to lack of experimental data, but realistically contact resistance plays a huge role in limiting device performance especially in wide band gap materials. It would be instructive to study the electrical interface properties of various metal contacts with c-BN material via DFT+NEGF simulation and incorporate the contact resistance information in the drift-diffusion simulation.

REFERENCES

[1] Siqi Shi, Jian Gao, Yue Liu, Yan Zhao, Qu Wu, Wangwei Ju, Chuying Ouyang, and Ruijuan Xiao. Multi-scale computation methods: Their applications in lithium-ion battery research and development. *Chinese Physics B*, 25(1):018212, 2015.

[2] Hyung-Wook Jeon, Heon-Phil Ha, Dow-Bin Hyun, and Jae-Dong Shim. Electrical and thermoelectrical properties of undoped Bi2Te3-Sb2Te3 and Bi2Te3-Sb2Te3-Sb2Se3 single crystals. *Journal of Physics and Chemistry of Solids*, 52(4):579–585, January 1991.

[3] Semiconductor Industry Association et al. International technology roadmap for semiconductors. *http://public. itrs. net/Files/2001ITRS/Home. htm*, 2001.

[4] CJ Sandroff, RN Nottenburg, J-C Bischoff, and R Bhat. Dramatic enhancement in the gain of a gaas/algaas heterostructure bipolar transistor by surface chemical passivation. *Applied Physics Letters*, 51(1):33–35, 1987.

[5] Wei Lu, Ping Xie, and Charles M Lieber. Nanowire transistor performance limits and applications. *IEEE transactions on Electron Devices*, 55(11):2859–2876, 2008.

[6] Lei Zhuang, Lingjie Guo, and Stephen Y Chou. Silicon single-electron quantum-dot transistor switch operating at room temperature. *Applied Physics Letters*, 72(10):1205–1207, 1998.

[7] Raymond Dingle, William Wiegmann, and Charles H Henry. Quantum states of confined carriers in very thin al x ga 1- x as-gaas-al x ga 1- x as heterostructures. *Physical Review Letters*, 33(14):827, 1974.

[8] Andre K Geim and Irina V Grigorieva. Van der waals heterostructures. *arXiv preprint arXiv:1307.6718*, 2013.

[9] Qing Hua Wang, Kourosh Kalantar-Zadeh, Andras Kis, Jonathan N Coleman, and Michael S Strano. Electronics and optoelectronics of two-dimensional transition metal dichalcogenides. *Nature nanotechnology*, 7(11):699–712, 2012.

[10] Likai Li, Yijun Yu, Guo Jun Ye, Qingqin Ge, Xuedong Ou, Hua Wu, Donglai Feng, Xian Hui Chen, and Yuanbo Zhang. Black phosphorus field-effect transistors. *Nature nanotechnology*, 9(5):372–377, 2014.

[11] L Britnell, RV Gorbachev, R Jalil, BD Belle, F Schedin, A Mishchenko, T Georgiou, MI Katsnelson, L Eaves, SV Morozov, et al. Field-effect tunneling transistor based on vertical graphene heterostructures. *Science*, 335(6071):947–950, 2012.

[12] Walter Kohn and Lu Jeu Sham. Self-consistent equations including exchange and correlation effects. *Physical review*, 140(4A):A1133, 1965.

[13] Dennis C Rapaport, Robin L Blumberg, Susan R McKay, Wolfgang Christian, et al. The art of molecular dynamics simulation. *Computers in Physics*, 10(5):456–456, 1996.

[14] John C Slater and George F Koster. Simplified lcao method for the periodic potential problem. *Physical Review*, 94(6):1498, 1954.

[15] Abraham Nitzan and Mark A Ratner. Electron transport in molecular wire junctions. *Science*, 300(5624):1384–1389, 2003.

[16] Carlo Jacoboni and Lino Reggiani. The Monte Carlo method for the solution of charge transport in semiconductors with applications to covalent materials. *Reviews of Modern Physics*, 55(3):645–705, July 1983.

[17] Mark S Lundstrom and Robert J Schuelke. Numerical analysis of heterostructure semiconductor devices. *IEEE Transactions on Electron Devices*, 30(9):1151–1159, 1983.

[18] Mohamed Hamid Elsheikh, Dhafer Abdulameer Shnawah, Mohd Faizul Mohd Sabri, Suhana Binti Mohd Said, Masjuki Haji Hassan, Mohamed Bashir Ali Bashir, and Mahazani Mohamad. A review on thermoelectric renewable energy: Principle parameters that affect their performance. *Renewable and Sustainable Energy Reviews*, 30:337–355, 2014.

[19] G Jeffrey Snyder and Eric S Toberer. Complex thermoelectric materials. *Nature materials*, 7(2):105–114, 2008.

[20] Osamu Yamashita, Shoichi Tomiyoshi, and Ken Makita. Bismuth telluride compounds with high thermoelectric figures of merit. *Journal of Applied Physics*, 93(1):368, December 2003.

[21] Mona Zebarjadi, Keivan Esfarjani, MS Dresselhaus, ZF Ren, and Gang Chen. Perspectives on thermoelectrics: from fundamentals to device applications. *Energy & Environmental Science*, 5(1):5147–5162, 2012.

[22] A. J. Minnich, M. S. Dresselhaus, Z. F. Ren, and G. Chen. Bulk nanostructured thermoelectric materials: current research and future prospects. *Energy & Environmental Science*, 2(5):466, May 2009.

[23] Abraham Fedorovich Ioffe. *Semiconductor thermoelements and thermoelectric cooling*. Infosearch, 1957.

[24] X. B. Zhao, X. H. Ji, Y. H. Zhang, T. J. Zhu, J. P. Tu, and X. B. Zhang. Bismuth telluride nanotubes and the effects on the thermoelectric properties of nanotube-containing nanocomposites. *Applied Physics Letters*, 86(6):062111, February 2005.

[25] Xinfeng Tang, Wenjie Xie, Han Li, Wenyu Zhao, Qingjie Zhang, and Masayuki Niino. Preparation and thermoelectric transport properties of high-performance p-type Bi[sub 2]Te[sub 3] with layered nanostructure. *Applied Physics Letters*, 90(1):012102, January 2007.

[26] Daryoosh Vashaee and Ali Shakouri. Improved Thermoelectric Power Factor in Metal-Based Superlattices. *Physical Review Letters*, 92(10):106103, March 2004.

[27] Gerald L. Pollack. Kapitza Resistance. *Reviews of Modern Physics*, 41(1):48–81, January 1969.

[28] P Giannozzi and *et al.* QUANTUM ESPRESSO: a modular and open-source software project for quantum simulations of materials. *Journal of physics. Condensed matter : an Institute of Physics journal*, 21(39):395502, September 2009.

[29] Rolf Landauer. Electrical resistance of disordered one-dimensional lattices. *Philosophical Magazine*, 21(172):863–867, September 2006.

[30] R. Mao, B. D. Kong, C. Gong, S. Xu, T. Jayasekera, K. Cho, and K. W. Kim. First-principles calculation of thermal transport in metal/graphene systems. *Physical Review B*, 87(16):165410, April 2013.

[31] Hongliang Shi, David Parker, Mao-Hua Du, and David J Singh. Connecting thermoelectric performance and topological-insulator behavior: Bi 2 te 3 and bi 2 te 2 se from first principles. *Physical Review Applied*, 3(1):014004, 2015.

[32] M Stordeur, M Stölzer, H Sobotta, and V Riede. Investigation of the valence band structure of thermoelectric (bi1- xsbx) 2te3 single crystals. *physica status solidi (b)*, 150(1):165–176, 1988.

[33] I. Bejenari and V. Kantser. Thermoelectric properties of bismuth telluride nanowires in the constant relaxation-time approximation. *Physical Review B*, 78(11):115322, September 2008.

[34] E. O. Kane. *Semicond. Semimetals*, 1:75, 1966.

[35] Jun Zhou, Xiaobo Li, Gang Chen, and Ronggui Yang. Semiclassical model for thermoelectric transport in nanocomposites. *Physical Review B*, 82(11):115308, 2010.

[36] Bao-Ling Huang and Massoud Kaviany. Ab initio and molecular dynamics predictions for electron and phonon transport in bismuth telluride. *Physical Review B*, 77(12):125209, March 2008.

[37] U. Sivan and Y. Imry. Multichannel Landauer formula for thermoelectric transport with application to thermopower near the mobility edge. *Physical Review B*, 33(1):551–558, January 1986.

[38] Sentaurus user's manual, synopsys, inc., 2015.

[39] Yuji Ando and Tomohiro Itoh. Calculation of transmission tunneling current across arbitrary potential barriers. *Journal of Applied Physics*, 61(4):1497, February 1987.

[40] S Sumithra, Nathan J Takas, Dinesh K Misra, Westly M Nolting, PFP Poudeu, and Kevin L Stokes. Enhancement in thermoelectric figure of merit in nanostructured bi2te3 with semimetal nanoinclusions. *Advanced Energy Materials*, 1(6):1141–1147, 2011.

[41] Dong-Kyun Ko, Yijin Kang, and Christopher B Murray. Enhanced thermopower via carrier energy filtering in solution-processable pt–sb2te3 nanocomposites. *Nano letters*, 11(7):2841–2844, 2011.

[42] Bed Poudel, Qing Hao, Yi Ma, Yucheng Lan, Austin Minnich, Bo Yu, Xiao Yan, Dezhi Wang, Andrew Muto, Daryoosh Vashaee, et al. High-thermoelectric performance of nanostructured bismuth antimony telluride bulk alloys. *Science*, 320(5876):634–638, 2008.

[43] Woochul Kim, Joshua Zide, Arthur Gossard, Dmitri Klenov, Susanne Stemmer, Ali Shakouri, and Arun Majumdar. Thermal conductivity reduction and thermoelectric figure of merit increase by embedding nanoparticles in crystalline semiconductors. *Physical Review Letters*, 96(4):045901, 2006.

[44] Kanishka Biswas, Jiaqing He, Ivan D Blum, Chun-I Wu, Timothy P Hogan, David N Seidman, Vinayak P Dravid, and Mercouri G Kanatzidis. High-performance bulk thermoelectrics with all-scale hierarchical architectures. *Nature*, 489(7416):414, 2012.

[45] Abram Fedorovich Ioffe. *Physics of semiconductors*. Infosearch, 1960.

[46] Jesse Maassen and Mark Lundstrom. A computational study of the thermoelectric performance of ultrathin bi2te3 films. *Applied Physics Letters*, 102(9):093103, 2013.

[47] Darshana Wickramaratne, Ferdows Zahid, and Roger K Lake. Electronic and thermoelectric properties of van der waals materials with ring-shaped valence bands. *Journal of Applied Physics*, 118(7):075101, 2015.

[48] Oded Rabina, Yu-Ming Lin, and Mildred S Dresselhaus. Anomalously high thermoelectric figure of merit in bi 1- x sb x nanowires by carrier pocket alignment. *Applied Physics Letters*, 79(1):81–83, 2001.

[49] Sang Il Kim, Kyunghan Ahn, Dong-Hee Yeon, Sungwoo Hwang, Hyun-Sik Kim, Sang Mock Lee, and Kyu Hyoung Lee. Enhancement of seebeck coefficient in bi0. 5sb1. 5te3 with high-density tellurium nanoinclusions. *Applied physics express*, 4(9):091801, 2011.

[50] Joseph P Heremans, Vladimir Jovovic, Eric S Toberer, Ali Saramat, Ken Kurosaki, Anek Charoenphakdee, Shinsuke Yamanaka, and G Jeffrey Snyder. Enhancement of thermoelectric efficiency in pbte by distortion of the electronic density of states. *Science*, 321(5888):554–557, 2008.

[51] Christopher M Jaworski, Vladimir Kulbachinskii, and Joseph P Heremans. Resonant level formed by tin in bi 2 te 3 and the enhancement of room-temperature thermoelectric power. *Physical Review B*, 80(23):233201, 2009.

[52] GD Mahan and JO Sofo. The best thermoelectric. *Proceedings of the National Academy of Sciences*, 93(15):7436–7439, 1996.

[53] Melvin Cutler and Nevill Francis Mott. Observation of anderson localization in an electron gas. *Physical Review*, 181(3):1336, 1969.

[54] John P Perdew, Kieron Burke, and Matthias Ernzerhof. Generalized gradient approximation made simple. *Physical review letters*, 77(18):3865, 1996.

[55] Stefan Grimme. Semiempirical gga-type density functional constructed with a long-range dispersion correction. *Journal of computational chemistry*, 27(15):1787–1799, 2006.

[56] BRK Nanda and I Dasgupta. Electronic structure and magnetism in doped semiconducting half-heusler compounds. *Journal of Physics: Condensed Matter*, 17(33):5037, 2005.

[57] SB Zhang and John E Northrup. Chemical potential dependence of defect formation energies in gaas: Application to ga self-diffusion. *Physical review letters*, 67(17):2339, 1991.

[58] Namita Narendra and Ki Wook Kim. Toward enhanced thermoelectric effects in bi2te3/sb2te3 heterostructures. *Semiconductor Science and Technology*, 32(3):035005, 2017.

[59] Deep Jariwala, Vinod K Sangwan, Lincoln J Lauhon, Tobin J Marks, and Mark C Hersam. Emerging device applications for semiconducting two-dimensional transition metal dichalcogenides. *ACS nano*, 8(2):1102–1120, 2014.

[60] Ruitao Lv, Joshua A Robinson, Raymond E Schaak, Du Sun, Yifan Sun, Thomas E Mallouk, and Mauricio Terrones. Transition metal dichalcogenides and beyond: synthesis, properties, and applications of single-and few-layer nanosheets. *Accounts of chemical research*, 48(1):56–64, 2014.

[61] Kin Fai Mak, Keliang He, Jie Shan, and Tony F Heinz. Control of valley polarization in monolayer mos2 by optical helicity. *Nature nanotechnology*, 7(8):494–498, 2012.

[62] Hannu-Pekka Komsa and Arkady V Krasheninnikov. Electronic structures and optical properties of realistic transition metal dichalcogenide heterostructures from first principles. *Physical Review B*, 88(8):085318, 2013.

[63] Kin Fai Mak, Changgu Lee, James Hone, Jie Shan, and Tony F Heinz. Atomically thin mos 2: a new direct-gap semiconductor. *Physical review letters*, 105(13):136805, 2010.

[64] Priya Johari and Vivek B Shenoy. Tuning the electronic properties of semiconducting transition metal dichalcogenides by applying mechanical strains. *ACS nano*, 6(6):5449–5456, 2012.

[65] Nengjie Huo, Jun Kang, Zhongming Wei, Shu-Shen Li, Jingbo Li, and Su-Huai Wei. Novel and enhanced optoelectronic performances of multilayer mos2–ws2 heterostructure transistors. *Advanced Functional Materials*, 24(44):7025–7031, 2014.

[66] Xiaoping Hong, Jonghwan Kim, Su-Fei Shi, Yu Zhang, Chenhao Jin, Yinghui Sun, Sefaattin Tongay, Junqiao Wu, Yanfeng Zhang, and Feng Wang. Ultrafast charge transfer in atomically thin mos2/ws2 heterostructures. *Nature nanotechnology*, 9(9):682–686, 2014.

[67] Christopher Muratore, Vikas Varshney, Jaime J Gengler, JJ Hu, John E Bultman, Timothy M Smith, Patrick J Shamberger, Bo Qiu, Xiulin Ruan, Ajit K Roy, et al. Cross-plane thermal properties of transition metal dichalcogenides. *Applied Physics Letters*, 102(8):081604, 2013.

[68] Yongji Gong, Junhao Lin, Xingli Wang, Gang Shi, Sidong Lei, Zhong Lin, Xiaolong Zou, Gonglan Ye, Robert Vajtai, Boris I Yakobson, et al. Vertical and in-plane heterostructures from ws2/mos2 monolayers. *Nature materials*, 13(12):1135–1142, 2014.

[69] Krzysztof Kośmider and Joaquín Fernández-Rossier. Electronic properties of the mos 2-ws 2 heterojunction. *Physical Review B*, 87(7):075451, 2013.

[70] E Cappelluti, Rafael Roldán, JA Silva-Guillén, Pablo Ordejón, and F Guinea. Tight-binding model and direct-gap/indirect-gap transition in single-layer and multilayer mos 2. *Physical Review B*, 88(7):075409, 2013.

[71] Gui-Bin Liu, Wen-Yu Shan, Yugui Yao, Wang Yao, and Di Xiao. Three-band tight-binding model for monolayers of group-vib transition metal dichalcogenides. *Physical Review B*, 88(8):085433, 2013.

[72] S Shallcross, S Sharma, E Kandelaki, and OA Pankratov. Electronic structure of turbostratic graphene. *Physical Review B*, 81(16):165105, 2010.

[73] B Ozpineci and LM Tolbert. *Comparison of wide-bandgap semiconductors for power electronics applications*. United States. Department of Energy, 2004.

[74] Chris JH Wort and Richard S Balmer. Diamond as an electronic material. *Materials Today*, 11(1):22–28, 2008.

[75] Satoshi Koizumi, Tokuyuki Teraji, and Hisao Kanda. Phosphorus-doped chemical vapor deposition of diamond. *Diamond and Related Materials*, 9(3):935–940, 2000.

[76] A Denisenko and E Kohn. Diamond power devices. concepts and limits. *Diamond and related materials*, 14(3):491–498, 2005.

[77] Jagdish Narayan and Anagh Bhaumik. Novel phase of carbon, ferromagnetism, and conversion into diamond. *Journal of Applied Physics*, 118(21):215303, 2015.

[78] Jagdish Narayan and Anagh Bhaumik. Novel synthesis and properties of pure and nv-doped nanodiamonds and other nanostructures. *Materials Research Letters*, 5(4):242–250, 2017.

[79] Jagdish Narayan, Anagh Bhaumik, and Weizong Xu. Direct conversion of h-bn into c-bn and formation of epitaxial c-bn/diamond heterostructures. *Journal of Applied Physics*, 119(18):185302, 2016.

[80] Julien Pernot and Satoshi Koizumi. Electron mobility in phosphorous doped {111} homoepitaxial diamond. *Applied Physics Letters*, 93(5):052105, 2008.

[81] Warren E Pickett. Thin superlattices and band-gap discontinuities: The (110) diamond–boron nitride interface. *Physical Review B*, 38(2):1316, 1988.

[82] Kazuo Yamamoto, Kazuaki Kobayashi, Toshihiro Ando, Mikka Nishitani-Gamo, Ryutaro Souda, and Isao Sakaguchi. Electronic structures of the diamond/boron-nitride interface. *Diamond and related materials*, 7(7):1021–1024, 1998.

[83] L Colombo, R Resta, and S Baroni. Valence-band offsets at strained si/ge interfaces. *Physical Review B*, 44(11):5572, 1991.

[84] XW Zhang. Doping and electrical properties of cubic boron nitride thin films: A critical review. *Thin Solid Films*, 544:2–12, 2013.

[85] Kwyro Lee, Michael S Shur, TJ Drummond, and H Morkoc. Currentvoltage and capacitancevoltage characteristics of modulation-doped field-effect transistors. *IEEE Transactions on Electron Devices*, 30(3):207–212, 1983.

[86] Subhasis Haldar and RS Gupta. 2-d analytical model for current–voltage characteristics and output conductance of algan/gan modfet. *Microwave and Optical Technology Letters*, 29(2):117–123, 2001.

[87] Ruixiang Fei, Alireza Faghaninia, Ryan Soklaski, Jia-An Yan, Cynthia Lo, and Li Yang. Enhanced thermoelectric efficiency via orthogonal electrical and thermal conductances in phosphorene. *Nano letters*, 14(11):6393–6399, 2014.

[88] Rui Mao, Yifeng Chen, and Ki Wook Kim. Atomistic modeling of phonon transport in turbostratic graphitic structures. *Journal of Applied Physics*, 119(20):204305, 2016.